Development and Application of Non-linear Mid-infrared Laser Spectroscopy for Combustion Diagnostics

Sun, Zhiwei

2012

Citation for published version (APA):
Sun, Z. (2012). *Development and Application of Non-linear Mid-infrared Laser Spectroscopy for Combustion Diagnostics*. [Doctoral Thesis (monograph), Combustion Physics].

LUND
UNIVERSITY

Department of Physics
Division of Combustion Physics

Development and Application of Non-linear Mid-infrared Laser Spectroscopy for Combustion Diagnostics

Zhiwei Sun

AKADEMISK AVHANDLING

som för avläggande av teknologie doktorsexamen vid tekniska fakulteten vid Lunds universitet kommer att försvaras vid offentlig disputation den 24 October 2012 klockan 10:15 i Hörsal B, Fysiska institutionen, Sölvegatan 14 C, Lund. Fakultetsopponent: Dr. Peter P. Radi, Paul Scherrer Institute, Switzerland

Organization LUND UNIVERSITY Division of Combustion Physics Department of Physics P.O. Box 118, SE-221 00 LUND, Sweden	Document name DOCTORAL DISSERTATION Date of issue Septempter 12, 2012 CODEN ISRN LUTFD2/TFCP-159-SE
Author(s) **Zhiwei Sun**	Sponsoring organization

Title and subtitle

Development and Application of Non-linear Mid-Infrared Laser Spectroscopy for Combustion Diagnostics

Abstract

The work reported in this thesis involved the development and application of two novel infrared non-linear laser techniques, namely mid-infrared polarization spectroscopy (IRPS) and mid-infrared degenerate four-wave mixing (IR-DFWM) to combustion diagnostics. These two techniques meet the needs of species concentration detection in combustion environments, especially for those species lacking accessible electronic (one-photon) transitions in the ultraviolet (UV) or visible spectral region. These species include many key molecules in combustion such as hydrocarbons (CmHn), H_2O, CO_2, HX (X = F, Cl and CN). Using IRPS or IR-DFWM, these important species can be in-situ and non-intrusively measured with a high spatial resolution by probing their ro-vibrational transitions in the mid-infrared, around 3 μm.

In terms of IRPS, this thesis mainly shows (1) the effective use of IRPS for measuring species (HCl, HCN, C_2H_2) concentration in atmospheric pressure clean or sooty flames, even in smoke/particles-laden environments during coal/biomass combustion; (2) the development of quantitative IRPS measurements considering collisional and quenching effects and spectral overlap coefficient; (3) the unique ability of species (HF) imaging in flames, working as a complementarity to planar laser-induced fluorescence commonly used in the UV/visible region.

As for IR-DFWM, a novel IR-beam-splitter set-up was developed, which provides a forward phase-matching geometry and greatly simplifies the alignment of an IR-DFWM system. This technique is firstly demonstrated for C_2H_2 and HCl detections in cold gas flow, and then it is applied for flame thermometry by monitoring the intensity ratios of H2O lines.

Both IRPS and IR-DFWM hold great potential for quantitative measurements of key molecular species important for combustion research, especially in low pressure flames, where collisional effects are considerably weaker. Moreover, these two techniques can be applied to other gas-phase diagnostics, such as in plasmas.

Key words
Combustion, Flame, Laser diagnostics, Non-linear laser spectroscopy, Mid-infrared, Polarization spectroscopy, Degenerate four-wave mixing, HITRAN, Concentration, Temperature

Classification system and/or index terms (if any)

Supplementary bibliographical information		Language English
ISSN and key title ISSN 1102-8718		ISBN 978-91-7473-356-3
Recipient´s notes	Number of pages **83**	Price
	Security classification	

Distribution by (name and address)

I, the undersigned, being the copyright owner of the abstract of the above-mentioned dissertation, hereby grant to all reference sources permission to publish and disseminate the abstract of the above-mentioned dissertation.

Signature Zhiwei Sun

Date **2012. 09. 12**

Development and Application of Non-linear Mid-infrared Laser Spectroscopy for Combustion Diagnostics

Doctoral Thesis

Zhiwei Sun

Division of Combustion Physics
Department of Physics

LUND 2012

LUND UNIVERSITY

Printed at Media Tryck AB, Lund, Sweden
September 2012

Lund Reports on Combustion Physics, LRCP 159
ISSN 1102-8718
ISRN LUTFD2/TFCP-159-SE
ISBN 978-91-7473-356-3

Zhiwei Sun
Division of Combustion Physics
Department of Physics
Lund University
P.O. Box 118
SE-221 00, Lund, Sweden

Abstract

The work reported in this thesis involved the development and application of two novel infrared non-linear laser techniques, namely mid-infrared polarization spectroscopy (IRPS) and mid-infrared degenerate four-wave mixing (IR-DFWM) to combustion diagnostics. These two techniques meet the needs of species concentration detection in combustion environments, especially for those species lacking accessible electronic (one-photon) transitions in the ultraviolet (UV) or visible spectral region. These species include many key molecules in combustion such as hydrocarbons (C_mH_n), H_2O, CO_2, HX (X = F, Cl and CN). Using IRPS or IR-DFWM, these important species can be in-situ and non-intrusively measured with a high spatial resolution by probing their ro-vibrational transitions in the mid-infrared, around 3 µm.

In terms of IRPS, this thesis mainly shows (1) the effective use of IRPS for measuring species (HCl, HCN, C_2H_2) concentration in atmospheric pressure clean or sooty flames, even in smoke/particles-laden environments during coal/biomass combustion; (2) the development of quantitative IRPS measurements considering collisional and quenching effects and spectral overlap coefficient; (3) the unique ability of species (HF) imaging in flames, working as a complementarity to planar laser-induced fluorescence commonly used in the UV/visible region.

As for IR-DFWM, a novel IR-beam-splitter set-up was developed, which provides a forward phase-matching geometry and greatly simplifies the alignment of an IR-DFWM system. This technique is firstly demonstrated for C_2H_2 and HCl detections in cold gas flow, and then it is applied for flame thermometry by monitoring the intensity ratios of H_2O lines.

Both IRPS and IR-DFWM hold great potential for quantitative measurements of key molecular species important for combustion research, especially in low pressure flames, where collisional effects are considerably weaker. Moreover, these two techniques can be applied to other gas-phase diagnostics, such as in plasmas.

List of papers

I. Z.S. Li, **Z.W. Sun**, B. Li, M. Aldén and M. Försth, *Spatially resolved trace detection of HCl in flames with mid-infrared polarization spectroscopy*, Optics Letters **33** (16) (2008) 1836-1838.

II. **Z.W. Sun**, J. Kiefer, Z.S. Li, B. Li and M. Aldén, *Four-wave mixing with non-resonant pump and resonant probe for OH detection in flames*, Applied Physics B-Lasers and Optics **92** (2) (2008) 287-293.

III. **Z.W. Sun**, Z.S. Li, B. Li, M. Aldén and P. Ewart, *Detection of C_2H_2 and HCl using mid-infrared degenerate four-wave mixing with stable beam alignment: towards practical in situ sensing of trace molecular species*, Applied Physics B-Lasers and Optics **98** (2-3) (2010) 593-600.

IV. **Z.W. Sun**, Z.S. Li, B. Li, Z.T. Alwahabi and M. Aldén, *Quantitative C_2H_2 measurements in sooty flames using mid-infrared polarization spectroscopy*, Applied Physics B-Lasers and Optics **101** (1-2) (2010) 423-432.

V. **Z.W. Sun**, Z.S. Li, A.A. Konnov and M. Aldén, *Quantitative HCN measurements in $CH_4/N_2O/O_2/N_2$ flames using mid-infrared polarization spectroscopy*, Combustion and Flame **158** (10) (2011) 1898-1904.

VI. **Z.W. Sun**, Z.S. Li, B. Li and M. Aldén, *Flame temperature diagnostics with water lines using mid-infrared degenerate four-wave mixing*, Journal of Raman Spectroscopy **42** (10) (2011) 1828-1835.

VII. **Z.W. Sun**, M. Försth, Z.S. Li, B. Li and M. Aldén, *Mid-infrared polarization spectroscopy: A tool for in situ measurements of toxic gases in smoke-laden environments*, Fire and Materials **35** (8) (2011) 527-537.

VIII. **Z.W. Sun**, J. Zetterberg, Z.S. Li, Z.T. Alwahabi and M. Aldén, *Spatially-resolved single-shot imaging in a flame using infrared polarization spectroscopy*, Submitted to Optics Letters.

IX. **Z.W. Sun**, Y. He, A.-L. Sahlberg, B. Li, Z.S, Li and M. Aldén, *Mid-infrared polarization spectroscopy applications in particle-laden combustion environments*, to be submitted.

Related papers

A. **Z.W. Sun**, N.J. Dam, Z.S. Li and M. Aldén, *NCN detection in atmospheric flames*, Combustion and Flame **157** (4) (2010) 834-836.

B. **Z.W. Sun**, M. Försth, Z.S. Li, B. Li and M. Aldén, *In situ measurements of HCN in a tube furnace with infrared polarization spectroscopy*, Fire Safety Science, **10**, (2011) 279-291.

C. **Z.W. Sun**, J.J. Zhu, Z.S. Li, M. Aldén, Y. Kusano, F. Leipold and M. Salewski, *Optical diagnostics of a gliding arc,* (to be submitted).

D. Bo Li, **Zhiwei Sun**, Zhongshan Li, Marcus Aldén, Jon G. Jakobsen, Stine Hansen and Peter Glarborg, *Post-Flame Gas-Phase Sulfation of Potassium Chloride*, (accepted by Combustion and Flame).

E. Z.S. Li, B. Li, **Z.W. Sun**, X.S. Bai and M. Aldén, *Turbulence and combustion interaction: High resolution local flame front structure visualization using simultaneous single-shot PLIF imaging of CH, OH, and CH_2O in a piloted premixed jet flame*, Combustion and Flame **157** (6) (2010) 1087-1096.

F. Johan Zetterberg, Sara Blomberg, Johan Gustafson, **Zhiwei Sun**, Zhongshan Li, Edvin Lundgren and Marcus Aldén, *An in situ set up for the detection of CO_2 from catalytic CO oxidation by using planar laser-induced fluorescence*, Review of Scientific Instruments **83** (2012) 053104.

G. O. Johansson, J. Bood, B. Li, A. Ehn, Z.S. Li, **Z.W. Sun**, M. Jonsson, A.A. Konnov and M. Aldén, *Photofragmentation laser-induced fluorescence imaging in premixed flames*, Combustion and Flame **158** (10) (2011) 1908-1919.

H. K. Tian, Z.S. Li, S. Staude, B. Li, **Z.W. Sun**, A. Lantz, M. Aldén and B. Atakan, *Influence of ferrocene addition to a laminar premixed propene* *flame: Laser diagnostics, mass spectrometry and numerical simulations*, Proceedings of the Combustion Institute **32** (2009) 445-452.

I. B. Li, E. Baudoin, R. Yu, **Z.W. Sun**, Z.S. Li, X.S. Bai, M. Aldén and M.S. Mansour, *Experimental and numerical study of a conical turbulent partially premixed flame*, Proceedings of the Combustion Institute **32** (2009) 1811-1818.

J. Z.H. Wang, L. Yang, B. Li, Z.S. Li, **Z.W. Sun**, M. Aldén, K.F. Cen and A.A. Konnov, *Investigation of combustion enhancement by ozone additive in* CH_4*/air flames using direct laminar burning velocity measurements and kinetic simulations*, Combustion and Flame **159** (1) (2012) 120-129.

K. Z.H. Wang, B. Li, A. Ehn, **Z.W. Sun**, Z.S. Li, J. Bood, M. Aldén and K.F. Cen, *Investigation of flue-gas treatment with* O_3 *injection using NO and* NO_2 *planar laser-induced fluorescence*, Fuel 89 (9) (2010) 2346-2352.

Contents

Chapter 1

Introduction

One sees combustion phenomena both in daily life and in industry applications, from simple candle lights to advanced gas-turbine aero engines. Combustion is still the major supplier of cheap and efficient energy to modern societies [1]. As a consequence combustion is a major source of carbon and other chemical pollutions. Combustion phenomena arise from complicated interactions of physical and chemical processes, involving mass and heat transport commonly entangled with turbulent fluid motions and sophisticated exothermal chemical reactions. For instance, even for the simplest H_2+O_2 flame, there are 21 elementary reactions in a reduced reaction mechanism [2]. Understanding the details of combustion is still challenging and crucial for improving combustion efficiency and reducing pollutant emissions, where both experimental measurements and numerical simulations play pivotal roles.

Complete understanding of complex combustion requires knowledge in many fields, such as chemical kinetics, fluid mechanics and thermodynamics. Thanks to the advent of modern computing power, sophisticated fluid mechanical models, such as large eddy simulation (LES) or direct numerical simulation (DNS) with detailed chemistry mechanisms, can be applied to simulate practical combustion systems in a more quantitative and predictive manner. This capacity for simulation requires reliable, quantitative and non-intrusive measurements to provide effective validations. Better diagnostics using new or refined measurement technologies are needed to generate useful data, to validate the success of combustors, or to identify potential failures [3] with the final goal being the control and optimization of the combustion processes.

Laser diagnostic techniques have for more than 30 years added very valuable input to both fundamental and applied combustion research. Different kinds of techniques have been developed for the measurements of important parameters, like temperature, species concentration, velocity and particle characteristics, with the ability to get detailed information in space and time. One of the main advantages with these techniques is that they are non-intrusive, i.e. measurements can be performed without introducing any physical probe, such as a thermocouple, that might influence the combustion by altering physical and chemical properties. Besides, these measurements can be performed with high spatial (about 10 - 50 μm) and temporal (< 10 ns) resolution [4].

On the whole, laser diagnostic techniques in combustion have largely focused on two research areas: (1) the development of new diagnostic techniques and (2) the application of mature techniques to laboratory flames and practical applications [4]. In order to measure new species or new parameters and perform measurements with greater accuracy and precision, novel laser techniques have continually been developed. The experimental research described in this thesis focused on the development and application of two infrared non-linear laser techniques: *polarization spectroscopy* (IRPS) and *degenerate four-wave mixing* (IR-DFWM).

Most of the laser diagnostic techniques for combustion studies have been applied in the UV/visible spectral region by exciting molecular electronic transitions. However, there are a number of important species involved in combustion that cannot be measured easily in this spectral region for various reasons, like the lack of accessible electronic transitions, or the high pre-dissociation rate at the upper electronic. In these instances, probing molecular ro-vibrational transitions by IR excitation becomes an attractive alternative for combustion diagnostics.

Being different from the line-of-sight absorption methods commonly available in the infrared spectral range, IRPS and IR-DFWM provide the capacity to conduct spatially precise measurements over the point defined by the crossing of two or three laser beams. Moreover, the signal beam generated in the two coherent techniques can be collected by detectors located remotely, which provides a sufficient discrimination against the background thermal IR radiation from hot reacting flows.

The focus of this thesis was to extend the application of IPPS to the detection of new species (HCl, HF and HCN) and to more challenging conditions (sooty and particle-laden combustion environments), to develop strategies for quantitative IRPS measurements, and to simplify the IR-DFWM set-up for practical applications. The outline of the thesis is as follows: some fundamentals of molecular spectroscopy and a very useful (for the work in this study) spectroscopic database (HITRAN) are given in Chapter 2 to offer the fundamentals for interpreting the recorded spectra; Chapter 3 provides the reader with a short description of the experimental equipment used in the research work; the theory, set-up and main results of IRPS measurements are discussed in Chapter 4; while those for the IR-DFWM are discussed in Chapter 5; a summary and outlook are finally described in Chapter 6. More detailed descriptions of the relevant works can be found in the attached papers at the end of the thesis.

Chapter 2

Molecular spectroscopy

Based on the *Born-Oppenheimer* approximation [5], the total energy E_{total} of a molecular system can be expressed separately in three parts

$$E_{total} = E_{electronic} + E_{vibration} + E_{rotation} \tag{2.0}$$

where $E_{electronic}$ is the electronic energy with a magnitude of about 1 - 10 eV, $E_{vibration}$ is the molecular vibration energy with a magnitude of around 0.1 eV and $E_{rotation}$ is the molecular rotational energy with a magnitude of around 10^{-3} eV. A schematic molecular level diagram is shown in Figure 2-1. $E_{electronic}$ refers to the electronic transitions mostly located in the UV/visible spectral range. $E_{vibration}$ refers to infrared transitions located mostly in the near or mid-infrared spectral range, while $E_{rotation}$ refers to microwave excitations.

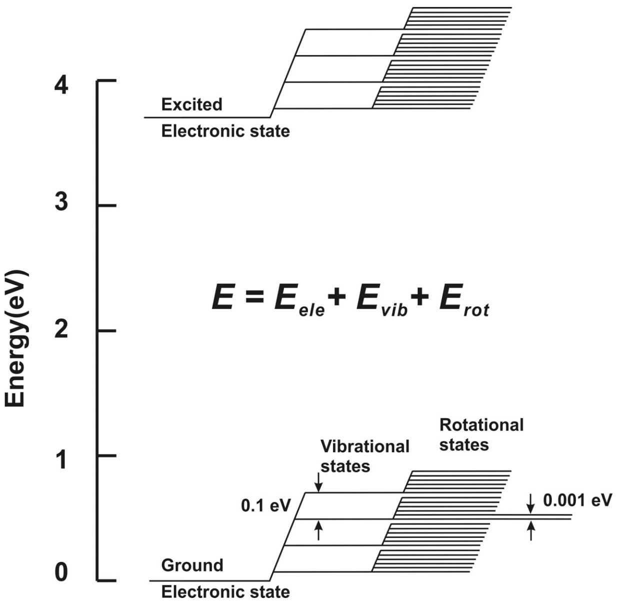

Figure 2-1 *Schematic molecular energy level diagram with electronic, vibrational and rotational levels. From [6].*

In the following sections, rotational spectroscopy and vibrational spectroscopy are discussed, followed by a brief discussion of electronic spectroscopy. Note that the following discussions are mainly about diatomic molecule to emphasize the physics but not the complicated mathematics. The HITRAN database (**hi**gh-resolution **tran**smission molecular absorption database) is introduced as a subsection for providing necessary molecular data when handling larger molecules. HITEMP as the high temperatures version of HITRAN will also be introduced.

2.1 Fundamental of molecular spectroscopy

2.1.1 Rotational spectroscopy

By using the Schrödinger equation the rotational energy levels allowed for a rigid diatomic molecule can be given as

$$E_J = \frac{h^2}{8\pi^2 I} J(J+1) \quad \text{joules}, \qquad (J = 0,\ 1,\ 2,\ \ldots) \tag{2.1}$$

where h is the Planck's constant, and I is the moment of inertia. The quantity J is called the *rotational quantum number*, taking integral values from zero upwards.

We rewrite Eq. (2.1) in the more frequently used spectral expression,

$$\varepsilon_J = \frac{E_J}{hc} = \frac{h}{8\pi^2 Ic} J(J+1) = BJ(J+1) \quad \text{cm}^{-1} \quad (J = 0,\ 1,\ 2, \ldots) \tag{2.2}$$

where B is called the *rotational constant*, and is given by

$$B = \frac{h}{8\pi^2 Ic} \tag{2.3}$$

The transitions between different levels of energy result in radiative emission or absorption, observed as spectra. However, these transitions do not happen randomly, i.e. some of them are forbidden by the *selection rule* for the rigid diatomic rotator

$$\text{Selection rule:} \qquad \Delta J = \pm 1 \tag{2.4}$$

therefore we have radiation at frequencies,

$$\upsilon_{J \to J+1} = 2B(J+1) \quad \text{cm}^{-1} \qquad (J = 0,\ 1,\ 2, \ldots) \tag{2.5}$$

Thus a rotational absorption spectrum will consist of lines at $2B$, $4B$, $6B$, … cm^{-1}. Note that this spectrum will only be observed for heteronuclear (asymmetric) molecules, like HCl and HF. While for homonuclear molecules, like N_2 and O_2, they have no dipole component change during rotational motion, hence no interaction with radiation. Moreover, the probability of all allowed transitions with $\Delta J = \pm 1$ is almost the same, meaning all are equally likely to happen. As a result, the intensities of spectral lines are directly proportional to the population of initial levels, determined by both the Boltzmann distribution and the degeneracy of the levels ($2J+1$).

The real diatomic molecules are non-rigid. When they rotates, centrifugal force will change the distance between the two nuclei. Considering another constant, the *centrifugal distortion constant* D, for a simple harmonic force field, the energy expression in Eq. (2.2) becomes

$$\varepsilon_J = BJ(J+1) - DJ^2(J+1)^2 \quad \text{cm}^{-1} \tag{2.6}$$

D is a positive quantity and can be expressed as

$$D = \frac{4B^3}{\varpi^2} \tag{2.7}$$

where ϖ is the *vibrational frequency.*

D is a constant in the order of 10^{-3} cm^{-1} which is much smaller than the B constant of around 10 cm^{-1}. Thus the correction part $DJ^2(J+1)^2$ is negligible when J is smaller than 5. Taking into account the distort correction, the transition frequency from J to $J+1$ is expressed as

$$\upsilon_{J\to J+1} = \varepsilon_{J+1} - \varepsilon_{J+1} = 2B(J+1) - 4D(J+1)^3 \quad \text{cm}^{-1} \tag{2.8}$$

And the selection rule, $\Delta J = \pm 1$, is kept.

The polyatomic molecules are to be discussed from the simple linear molecules to symmetric top molecules. Asymmetric molecules, due to their complexity, are not considered. In order to simplify the discussion, the rotation is resolved into three mutually perpendicular directions through the principal axes of rotation. Three *principle moments of inertia*, therefore, are denoted as I_A, I_B, I_C, and appear along each axis.

Linear molecules (HCN, OCS)

Since I_B = I_C and I_A = 0, the energy expression is identical to that of diatomic molecules, like Eq. (2.6), and the section rule of $\Delta J = \pm 1$ is also kept. Note that the B constant is less than that for diatomic (10 cm^{-1}) and the spectral lines are more closely spaced. It can be less than 1 cm^{-1} for triatomic molecules, and the larger the molecule, the smaller the B constant.

Symmetric top molecules (NH_3, CH_3Cl)

I_B = I_C ≠ I_A, I_A ≠ 0; it is conventional to use J to represent the *total angular momentum* and to use K to represent the angular momentum about the top axis, i.e. about the C-Cl bond in the case of CH_3Cl. K takes the values:

$$K = J,\ J-1,\ J-2,\ \ldots,\ 0,\ \ldots\ -(J-1),\ -J \tag{2.9}$$

The energy levels for rotation are

$$\varepsilon_{J,K} = BJ(J+1) + (A-B)K^2 \quad \text{cm}^{-1} \tag{2.10}$$

where $B = \dfrac{h}{8\pi^2 I_B c}$ and $A = \dfrac{h}{8\pi^2 I_A c}$.

The selection rules are

$$\Delta J = \pm 1 \text{ and } \Delta K = 0 \tag{2.11}$$

That results in a spectrum with frequency

$$\upsilon_{J,K} = \varepsilon_{J+1,K} - \varepsilon_{J,K} = 2B(J+1) \quad \text{cm}^{-1} \tag{2.12}$$

Note that in Eq. (2.12), the spectrum is independent of K, meaning rotational changes about the symmetry axis do not induce any rotational spectrum.

Spherical top molecules (CH_4, SF_6)

I_B = I_C = I_A; Pure rotation does not produce any dipole change and hence no rotational spectrum appears.

Asymmetric molecules (H_2O)

Due to their much more complicated energy levels and spectra, asymmetric molecules will not be discussed in this thesis. However, we can extract the detailed spectral information from the HITRAN/HITEMP database. See section 2.2.

2.1.2 Vibrational spectroscopy

For simplicity, we also here start with diatomic molecules. The anharmonic oscillator model is always employed to describe the vibration of diatomic molecules, and the allowed energies are

$$\varepsilon_v = (v+\frac{1}{2})\varpi_e - (v+\frac{1}{2})^2 \varpi_e x_e \quad \text{cm}^{-1} \qquad (v = 0,\ 1,\ 2,\ldots) \tag{2.13}$$

where ϖ_e is an *oscillation frequency* and x_e is the corresponding *anharmonicity constant* which is positive, hence the vibrational levels becomes crowded with increasing v (the rotational levels becomes sparse with increasing J). The selection rules for the anharmonic oscillator are

$$\Delta v = \pm 1,\ \ \pm 2,\ \ \pm 3,\ldots \tag{2.14}$$

and the frequency for these transition are

$$\begin{array}{lll} \Delta v = +1 & \Delta\varepsilon = \varpi_e(1-2x_e) & \text{cm}^{-1} \\ \Delta v = +2 & \Delta\varepsilon = 2\varpi_e(1-3x_e) & \text{cm}^{-1} \\ \Delta v = +3 & \Delta\varepsilon = 3\varpi_e(1-4x_e) & \text{cm}^{-1} \end{array}$$

x_e is very small, about 0.01, and three spectral lines near ϖ_e , $2\varpi_e$ and $3\varpi_e$, are called *fundamental absorption*, the *first* and the *second* overtones, respectively

Considering the detailed rotational levels in each vibrational level as shown in Figure 2-1, the allowed level energies are

$$\varepsilon_{J,v} = BJ(J+1) + (v+\frac{1}{2})\varpi_e - (v+\frac{1}{2})^2 \varpi_e x_e \quad \text{cm}^{-1} \tag{2.15}$$

Note that the D constant in Eq. (2.6) is ignored in Eq. (2.15) due to its minor effect on the spectrum. However, the *Born-Oppenheimer* approximation does not always hold, and we need to take into account another effect, that of the interaction of rotations and vibrations. Every vibrational level has its own B constant, denoted as B_v, for the corresponding rotational levels.

$$B_v = B_e - \alpha(v+\frac{1}{2}) \tag{2.16}$$

where α is a small positive constant. For example, α = 0.018 for the CO fundamental band around 2130 cm^{-1}. Eq. (2.16) indicates that an increase in vibrational energy will lead to an increase in the average bond length, hence a smaller B constant.

The selection rules are

$$\Delta v = \pm 1,\ \ \pm 2,\ \ldots \text{and}\ \ \Delta J = \pm 1 \tag{2.17}$$

The frequencies of fundamental transitions $v = 0$ to $v = 1$ are

$$\Delta\varepsilon = \varepsilon_{J',v=1} - \varepsilon_{J'',v=0} = \varpi_0 + B_1 J'(J'+1) - B_0 J''(J''+1) \tag{2.18}$$

where $\varpi_0 = \varpi_e(1-2\chi_e)$ is defined as before. The changes in the rotational quantum number ΔJ = -1 (i.e. $J'=J''-1$) and ΔJ = 1 (i.e. $J'=J''+1$) result in two branch lines, called *P-branch* and *R-branch*, respectively. A simplified equation can express these line frequencies as

$$\upsilon_{P,R} = \varpi_0 + (B_1 + B_0)m + (B_1 - B_0)m^2 \quad \text{cm}^{-1} \qquad (m = \pm 1,\ \pm 2, \ldots) \tag{2.19}$$

where the negative m values refer to the P-branch and the positive to the R-branch. No Q-branch appears in the ro-vibrational spectra of diatomic molecules.

The vibrations of polyatomic molecules have several fundamental modes, like symmetric stretching mode, asymmetric stretching modes and bending mode. Below, the combinations of the vibrational transitions with rotational transition, i.e. ro-vibrational transitions of polyatomic molecules, are discussed.

Linear molecules (HCN, OCS)

Parallel vibrations: The section rule is identical with that of diatomic molecules.

$\Delta J = \pm 1,\ \ \Delta v = \pm 1$ for *simple harmonic motion*
$\Delta J = \pm 1,\ \ \Delta v = \pm 1,\ \pm 2, \ldots$ for *anharmonic motion*

Perpendicular vibrations: The selection rule is

$\Delta J = 0, \pm 1,\ \ \Delta v = \pm 1$ for *simple harmonic motion*

and the transitions of ΔJ = 0 result in a Q-branch, appearing between the P- and the R-branch. The frequencies for Q-branch lines are

$$\Delta\varepsilon = \varepsilon_{J',v=1} - \varepsilon_{J'',v=0} = \varpi_0 + J(J+1)(B_1 - B_0) \tag{2.20}$$

According to Eq. (2.16) (B_1-B_0) is so small that Q-branch appears as a somewhat broadband structure. One thing noted here is that polyatomic molecules with zero dipole moment (CO_2, C_2H_2, CH_4) do not have pure rotation spectra as discussed; however, they have vibrational spectra in the infrared. Interestingly, spectra of CO_2 and C_2H_2 have *special* structures due to the influence of *nuclear spin* that is an additional factor determining the populations of rotational levels. CO_2 has a line spacing of 4*B* rather than 2*B* as usual. P- and R-branch lines of C_2H_2 show a strong-weak-repeating structure with an intensity ratio of 3:1 that is observed to be 9:1 in our non-linear techniques, see *Paper* III.

Symmetric top molecules (NH_3, CH_3Cl)

The energies of the allowed levels are

$$\varepsilon_{J,v} = (v+\frac{1}{2})\varpi_e - (v+\frac{1}{2})^2 \varpi_e x_e + BJ(J+1) + (A-B)K^2 \qquad (2.21)$$

And the selection rules are

$\Delta v = \pm 1,\ \Delta J = 0, \pm 1,\ \Delta K = 0$ for parallel vibrations

$\Delta v = \pm 1,\ \Delta J = 0, \pm 1,\ \Delta K = \pm 1$ for perpendicular vibrations

2.1.3 Electronic spectroscopy

Most work for the current research was performed in the mid-infrared. Electronic transitions, resulting in spectral lines in the UV or visible range, were seldom involved, therefore only a brief introduction for electronic spectroscopy is included here.

According to the *Born-Oppenheimer* approximation and being similar to the former discussion, an electronic energy, ε_{elec}, is added into the energy formula for the molecule. ε_{elec} is normally in the order of 1 - 10 eV, which brings the electronic spectra in the UV or visible range. Combined with electronic transitions, transitions between rotation and vibration levels in different electronic levels also happens, therefore, broadband but line-structure electronic spectra appear for diatomic molecules. The shape of electronic band is dependent on the *Franck-Condon* principle [5], and sometimes continuum spectra appear. Also due to the large difference between the rotational constant *B* in the two related electronic levels, band head exists in spectra.

The structure of electronic levels is much more complicated. Only the selection rules for *diatomic* molecules are summarized here.

1) The total orbital angular momentum: $\Delta\Lambda = 0, \pm 1$.

   Only transitions between Σ - Σ, Σ - Π *etc.* are allowed.

2) The total spin momentum: $\Delta S = 0$

3) The electronic angular momentum: $\Delta\Omega = 0, \pm 1$.

4) There are also restrictions on symmetry changes, i.e.

   (+ *to* +), (- *to* -), (+ *not to* -), and (*g only to u*).

2.2 The HITRAN/HITEMP database

In *section 2.1*, the fundamentals of molecular spectroscopy, mainly rotational and vibrational spectroscopy, were briefly introduced. This basic knowledge helps us to understand the structure of existing spectra, or to simulate the spectra for simple molecules, like CO, based on their molecular constants *B*, *D*, $\varpi_e\chi_e$, ϖ_e, ϖ_0 and so on. However, in the author's experience, it is not always convenient or practical to predict the spectral parameters needed, especially when the studied molecule is polyatomic or is not linear or symmetric in structure. It is very hard, or even impossible for normal users to get quantitative information about spectral lines, like their absorption cross section. In this case, the well-known spectroscopic database, HITRAN, becomes very helpful in identification of the spectral lines from measured spectra.

The HITRAN database, being free of charge and available at *http://www.cfa.harvard.edu/hitran/*, is the recognized international standard spectroscopic database, from which a wide variety of computer simulation codes are able to calculate and predict the transmission and emission spectra of many atmospheric molecules. The database is widely used in activities such as remote sensing in astronomy, transmission simulations, fundamental laboratory spectroscopy studies and industrial process monitoring. It is a prominent and long running project started by the *Air Force Cambridge Research Laboratories* (AFCRL) in the late 1960's in response to the need for detailed knowledge of the infrared properties of the atmosphere. The original version of the database appeared as a report in 1973, only including seven principle atmospheric molecules (H_2O, CO_2, O_3, NO, CO, CH_4 and O_2) containing more than 100,000 lines from less than 1 μm to the far infrared. The parameters included for each line were: frequency, intensity, half-width, energy of the lower state of the transition, vibrational and rotational identification of the upper and lower energy states, an isotopic identification and a molecular identification.

After 40 years development the current version, HITRAN2008 [7], includes 42 species with more than 4.7×10^6 spectral lines. It also includes many more spectroscopic parameters for *every* line listed, as seen in Table 1. The important feature for the HITRAN database is the *line-by-line* portion. We can extract the parameters listed in Table 1 for every single line directly, rather than calculate them based on the basic spectroscopic constants.

Table 1. Variables in the HITRAN2008 database

Variable	**Units**	**Definition**
Mol	unitless	Molecule number
I_a	unitless	Isotopologue number
v	cm^{-1}	Transition wavenumber
S	cm^{-1}/(molecule cm^{-2})	Intensity at 296 K
A	s^{-1}	Einstein A-coefficient
γ_{air}	$cm^{-1}atm^{-1}$	Air-broadened half-width at 296 K
γ_{self}	$cm^{-1}atm^{-1}$	self-broadened half-width
E''	cm^{-1}	Lower state energy
n_{air}	unitless	Temperature-dependence exponent of r_{air}
δ_{air}	$cm^{-1}atm^{-1}$	Air pressure-induced shift
v', v''	unitless	Upper- and lower-state *global* quanta
q', q''	unitless	Upper- and lower-state *local* quanta
ierr	unitless	Uncertainty indices
iref	unitless	Reference indice
g', g''	unitless	Upper- and lower-state statistical weights

In Appendix *A* of publication [8], i.e. the special issue for HITRAN'96, very detailed definitions of the variables listed in Table 1 were provided. Some points that should be noted are:

1) The spectral intensity S is defined for a single molecule, already considering the degeneracy of the state (i.e. g', g'', the state statistical weights). Moreover, S has been weighted according to the natural terrestrial isotopic abundances that are available in the file named *MOLPARAM.txt* in the website of HITRAN.

2) The HITRAN database is often used for transmission simulations, but it can also be used for emission simulations, for example, simulating the flame radiation, since the Einstein A-coefficient is also included. It should be noted that the statistical weights of the upper state should be accounted for by users.

3) The temperature dependent parameters listed in the database refer 296 K. Since the population partition between states is the function of temperature through Boltzmann statistics, a temperature correction of the line intensity should be performed when the database is used for high temperature gaseous molecules. Eq. (A11) in appendix A [8] can be used.

For the current research, the HITRAN database was always used for *spectral line identification* and *concentration quantification*. In the first instance, the parameter v (line frequency) helped to identify the spectral lines of target species in recorded spectra. The spectral lines of target species could be interfered by the lines from other major species in flames, like H_2O and CO_2, whose spectra can be simulated with the help of the HITRAN database. And when planning experiments, it is wise to simulate simultaneously the spectra of the target species and those of the species that may initiate spectral interferences. This preparation assists in choosing the spectral region where measurements can be well performed. In the second instance, the parameter S was always extracted from the HITRAN database as a function of temperature, and applied to calculate the species concentration from the recorded signal intensity.

While there is line width information in the HITRAN database, when a spectrum was simulated in the current study, the information (γ_{air}, γ_{self}) from HITRAN was not adopted. The kind of information was not used because the buffering gases in flames are somewhat different from those in ambient air (mainly N_2 and O_2). In spectra simulations, the line width is adjusted manually to be consistent with the measured spectra. Furthermore the Doppler broadening effect is much less in the infrared compared to the UV/visible range.

Figure 2-2 shows the IRPS spectrum recorded in a sooty ethylene/air flame, where acetylene (C_2H_2) exists and plays an important role in soot formation. A simulated IRPS spectrum for pure C_2H_2 at 1800 K based on HITRAN2008 is shown as well. There are distinct discrepancies between measured and simulated spectra for C_2H_2. (Please note the strong lines in measured spectra are for H_2O molecules). The reason for this difference between measured and simulated spectra remains unclear.

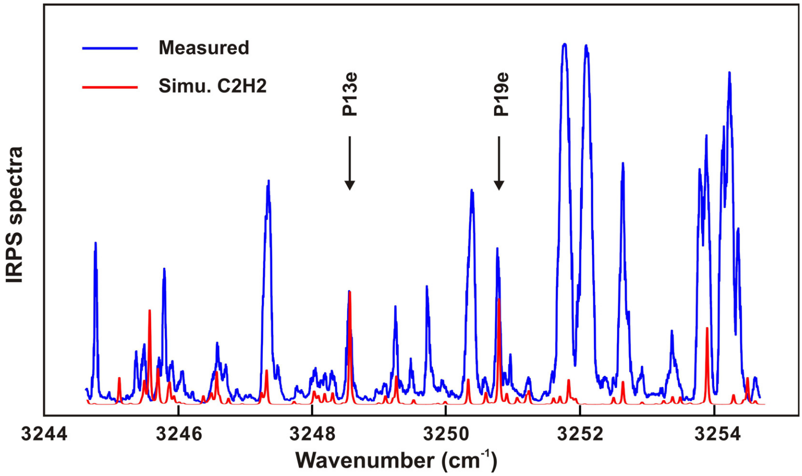

Figure 2-2 *IRPS spectrum (in blue) recorded in a sooty ethylene/air flame with the equivalence ratio of 2.1 in the McKenna burner. The measured point is 9 mm above the burner surface. Simulated IRPS spectrum (in red) for pure* C_2H_2 *at 1800 K is also shown.*

The HITRAN database, established at a reference temperature of 296 K, does not work well for gases at elevated temperatures. Although in HITRAN the scaling from room temperature to high temperatures is sufficiently accurate to estimate the line intensity at higher temperature, providing an adequate high-temperature partition, the additional spectral lines that are missing in HRITAN often lead to a significant underestimation of the source radiance in specific spectral regions [9]. In terms of the current study, the missing lines in HITRAN at flame temperatures consistently made spectral line identification more difficult.

An analogous spectroscopic database has been established, namely HITEMP [9, 10], for high-temperature modelling of the spectra of the gas-phase molecules. The HITEMP database is also available at http://www.cfa.harvard.edu/hitran/. The current version HITEMP2010 [9] maintains the same format as that used for HITRAN but encompasses many more bands and transitions than HITRAN for H_2O, CO_2, CO, NO and OH (see Table 2).

The HITRAN/HITEMP databases provide useful spectroscopic data in IRPS and IR-DFWM research. These kinds of spectroscopic databases have being constructed for different purpose with the help of rapid development of internet services. In work [11] a database named Virtual atomic and molecular data centre (VAMDC, http://www.vamdc.eu) was introduced, where different databases available for atmospheric science, astrochemistry, plasma, lighting, fusing energy research and radiation science were briefly described.

The HITRAN/HITEMP databases proved useful in IRPS and IR-DFWM research in terms of line position and intensity. Meanwhile, IRPS and IR-DFWM also have the potential of extending these two spectroscopic databases, since the techniques developed in the course of the current study can be run in sub-Doppler geometry providing high-resolution spectral measurements, especially at high temperatures.

Table 2. Line list comparison between HITEMP2010 and HITRAN2008 [9]

Molecules	Spectral coverage (cm^{-1})	Number of transitions		Dissociation energy (cm^{-1})
		HITEMP2010	HITRAN	
H_2O	0-30,000	111,377,777	69,201	41,145.94
CO_2	258-9648	11,167,618	312,479	44,360
CO	0-8465	115,218	4,477	90,674
NO	0-9274	105,633	105,079	52,265
OH	0-19,268	40,055	31,976	35,593

Chapter 3

Experimental equipment and objects

3.1 Light source

The laser system used for most of the investigations in the current research consisted of an injection seeded Nd:YAG laser, a dye laser and a frequency conversion unit. The dye laser is pumped by the 532 nm frequency-doubled output of the Nd:YAG laser. The tunable output in the near-infrared is differential frequency-mixed with part of the residual of the 1064 nm output from the Nd:YAG laser in the frequency conversion unit to generate the mid-infrared laser emission determined by $\omega_{IR} = \omega_{dye} - \omega_{1064nm}$. These three parts, i.e. the Nd:YAG laser, the dye laser and the frequency conversion unit, are described in detail below.

3.1.1 Nd:YAG laser

The Nd:YAG laser is one of the most commonly used high-power pulsed lasers. It is a solid-state laser with the fundamental output fixed at 1064 nm. Frequency-conversion provides doubling, tripling and quadrupling laser beams at 532 nm, 355 nm and 266 nm, respectively. The Nd:YAG laser can work directly for some diagnostic techniques, such as Rayleigh and Raman scattering, laser-induced incandescence (LII), laser-induced phosphorescence (LIP) and particle image velocimetry (PIV). It can even be used for laser-induced fluorescence (LIF) of some important fuels or transient species, such as fuel visualization using 266 nm and formaldehyde imaging using 355 nm. In addition, the Nd:YAG laser can be used as the pumping light source for other tunable frequency extension laser systems, like dye lasers and optical parametric oscillators (OPO).

An injection seeded, single-longitudinal-mode Nd:YAG (Spectra Physics, Quanta-Ray PRO 290-10) is employed, operating at a repetition rate of 10 Hz and with a pulse duration of 8 - 10 ns at the fundamental output. This laser has a narrow line width better than 0.003 cm^{-1}. The doubling output, around 700 mJ/pulse, is used to pump the dye laser, while part of the residual 1064 nm beam after the frequency doubling is sent into the frequency conversion unit. The model 6350 injection seeder is installed in the Nd:YAG laser.

3.1.2 Dye laser

A Sirah PrecisionScan PRSC-D-18 dye laser is pumped by the Nd:YAG laser. The dye laser is equipped with a double grating resonator, with 1800 lines/mm gratings and a second amplifier option. Working with different dye, the dye laser has a tuning range of 410 – 900 nm, a line width specified to 0.05 cm^{-1} at 625 nm. A pulsed energy of 50 – 60 mJ is achieved at 800 nm.

3.1.3 Frequency conversion unit

A Sirah Near Infra-Red Optical Parametrical Amplifier unit (OPANIR) is employed to generate powerful laser radiation in the mid-infrared to excite the target species. The dye laser output beam and a fraction of the residual 1064 nm beam from the Nd:YAG are mixed in a $LiNbO_3$ crystal regulated at 70 °C for difference frequency generation. The $LiNbO_3$ crystal covers the range 1.8 - 3.8 µm determined by the cutting angle. The generated infrared laser beam is further amplified in a second $LiNbO_3$ crystal pumped by the residual of the 1064 nm laser beam, working as an optical parametric amplifier (OPA).

The pulsed output energy after the OPA amplifier varies from 2 to 8 mJ (at 3 µm) depending on the energy of the Nd:YAG laser and the dye laser due to the non-linear generation process. By using different dyes, a wide tunable range can be achieved, as shown in Figure 3-1. The resulting bandwidth is mainly governed by the dye laser, since the bandwidth of the injection seeded Nd:YAG is much narrower. A bandwidth of less than 0.04 cm^{-1} at 3.4 µm was estimated from the line width of the dye laser (0.03 cm^{-1} specified by the manufacturer). A typical full-width-half-maximum (FWHM) line width, 0.025 cm^{-1} at 2.7 µm, was measured using an excitation scan of IR laser-induced fluorescence (LIF) of CO_2 in a 10 mbar gas cell, by fitting the LIF spectrum, taking into account both Doppler broadening ($\approx$ 0.0067 cm^{-1} FWHM) and collisional broadening (< 0.002 cm^{-1} FWHM) [12]. The polarization of the mid-infrared laser beam is horizontal and a half-wave plate (to be discussed in *section 3.2.3*) is employed to rotate it to vertical. The laser pulse duration is approximately 4 ns.

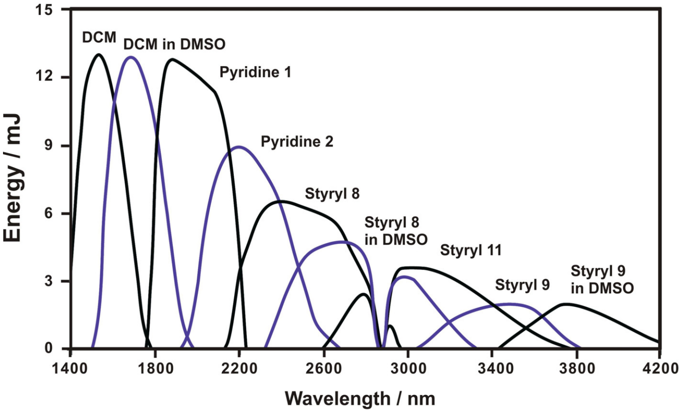

Figure 3-1 *Tuning curves for frequency conversion unit with approximately 500 mJ@532 nm pump energy. (from: http://www.photonicsolutions.co.uk).*

3.2 Optics components

3.2.1 Infrared optics

In the mid-infrared spectral range, on which most of the current study was focused, silica-based optics materials, like BK7 and fused silica, have low transmittance. Therefore other optical materials with effective transmittance in that range had to be adopted. In Figure 3-2, the transmittances of commonly used infrared material are shown. CaF_2, sapphire and MgF_2 have good transmittance in the spectral region of interest. Therefore, the windows or dichroic mirrors made of these materials, in particular CaF_2 and sapphire, were always applied in our set-up.

These infrared windows also work as beam splitters, reflecting part of the laser beam, working as the probe beam. The refractive index values of the chosen material are required since different materials will produce different reflections. A very useful database is available at *http://refractiveindex.info* where refractive index values for calculating the reflections of different infrared optical materials can be found as a function of the wavelength, the incident angle and the polarization of the incident light.

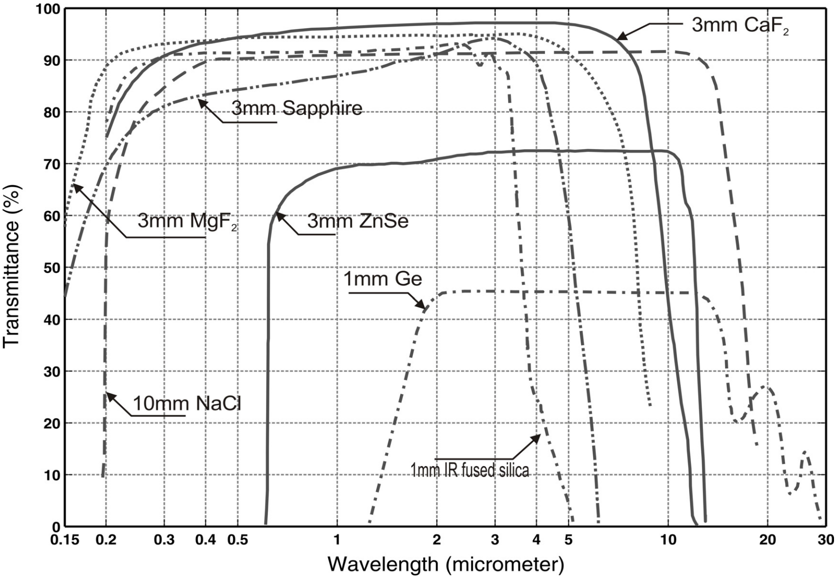

Figure 3-2 *Transmittances of typical infrared optical materials. (The curves are based on the information from www.newport.com).*

3.2.2 Polarizer

The polarizer is one of the most crucial parts in a PS set-up, since a zero or near-zero background is crucial for viewing the relative week PS signal. Three types of polarizers, i.e. Glan-laser polarizer, Glan-Taylor polarizer and Glan-Thompson polarizer, can be used in a PS set-up to create polarization purity due to their high extinction ratio of up to 10^7:1. These polarizers are made of two prisms which are assembled with air space for the Glan-laser and Glan-Taylor polarizers or without any space for a Glan-Thompson polarizer. Unlike the Glan-Taylor polarizer, the Glan-laser polarizer contains an exit aperture to provide safe escape windows for the beam of the rejected polarization. This feature makes the Glan-laser polarizer more desirable when using a high energy laser.

Figure 3-3 presents a schematic of the type of Glan-laser polarizer employed in the probe beam of the IRPS set-up. The two pieces of prisms are made of YVO_4 (Yttrium Vanadate) crystal with a clear aperture of 15×15 mm^2 which is necessary for two-dimensional (2D) IRPS, as discussed in *Paper* VIII. The antireflective coating on the polarizer reduces light loss on the collection window. Normally the polarizers are used in the scheme of 0° incident angle (i.e. the light is perpendicular to the polarizer window). The extinction ratio of this pair of polarizers was measured to be 10^7:1 when they were fresh; however, we noted that this became worse after years of usage. The polarizers were mounted on fine rotators, which could be used to adjust the cross angle between the two polarizer axes, as well as the angle to incident light.

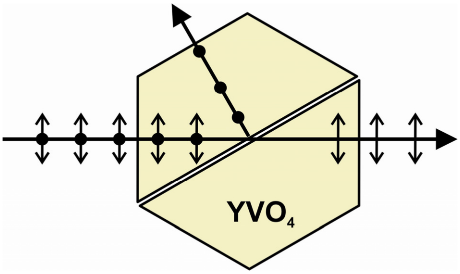

Figure 3-3 *Schematic of a Glan-laser polarizer used in this thesis, and its function on the laser polarizations.*

3.2.3 Tunable wave plate

A PS set-up involves a linearly polarized probe beam and a circularly or linearly (45° rotated to the polarization of the probe beam) polarized pump beam. Therefore the polarization of both beams required adjustments for the current study. In our IRPS set-up, zero-order tunable quarter-wave or half wave phase retardation plates (ALPHALAS GmbH) are used to vary the polarization of the beams, as shown in Figure 3-4. A circularly polarized beam prepared using a quarter-wave plate, or a linearly polarized beam rotated to a specified angle using a half-wave plate, can be produced from a linearly polarized beam.

This tunable phase retardation plate features a very wide bandwidth of 260 nm at 3 µm. It works for an arbitrary wavelength from 150 nm to 6 µm, by tuning the angle of θ as shown in Figure 3-4 according to the tuning curve (θ as a function of beam wavelength) provided by the manufacture. With a thickness of 2 mm, this plate does not change much of the passing beam direction. A half-wave plate was also used to change the polarization of the original laser beam (directly from the frequency conversion unit) from horizontal to vertical.

3.2.4 Novel beam splitter

A novel beam splitter was developed to facilitate the IR-DFWM technology. The beam splitter can split a single input IR laser beam into four parallel beams with

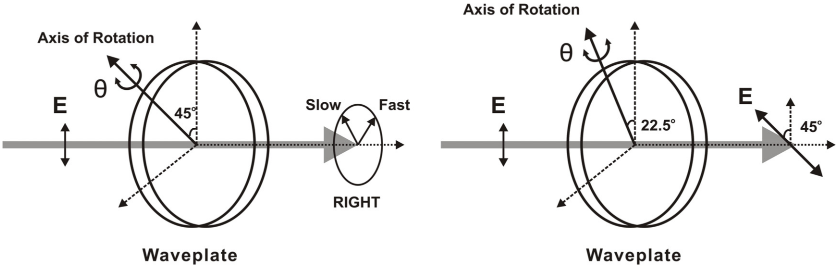

Figure 3-4 *Zero-order tunable quarter-wave and half-wave phase retardation plate, changing the vertical polarized light beam to be right-circularly polarized or linear polarizer with 45° rotated.*

similar intensity. These beams can then be focused together by a single lens to conveniently realize the forward phase-matching geometry for DFWM.

The infrared beam splitter is composed of two identical parallel-sided plates similar to those used in previous works [13, 14], and is shown schematically in Figure 3-5. The accurately parallel-sided plates are CaF_2 with a dimension of $50\times50\times15$ mm^3. They are coated with anti-reflecting, 50% reflecting and high reflecting (> 95%) layers over the areas shown in the diagram. The horizontally propagating single infrared input beam is incident on the first plate which is tilted at an angle of 45°. The input and output facets are anti-reflection coated; the first internal reflection facet is coated to yield 50% reflection and the second internal reflection facet is coated to yield high reflection. The coatings were prepared for a spectral range 2.7 - 3.3 μm (3000 - 3700 in cm^{-1}). One input beam can thus be split into two parallel beams of almost equal intensity. Each beam can then be split into two beams using the second, identically prepared plate. This second plate is tilted by 45° about an axis perpendicular to that of the first. Fine adjustment of the

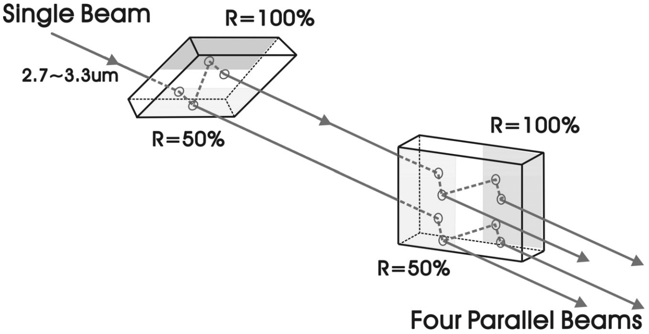

Figure 3-5 *Beam splitter designed for IR-DFWM. The incident angle of beam to the plate is 45 degrees.*

angles of incidence on the beam splitters at 45° results in four parallel beams distributed to four corners of a 12×12 mm^2 rectangle with almost equal intensity.

3.3 Detectors

3.3.1 InSb detector

Indium Antimonide (InSb) point detector (Teledyne Judson technologies, type: J10D-M204-R04M-60) is employed in the IPRS and IR-DFWM set-up due to its excellent performance in the 1 to 5.3 μm wavelength range. This InSb detector requires a 77 K operating temperature; therefore liquid N_2 is needed for cooling. This type of InSb detector has a round, active sensing area 4 mm in diameter. The signal from the InSb detector is amplified by a PA-9 trans-impedance preamplifier with a bandwidth of 15Hz to 574 kHz.

The background noise is a crucial parameter for sensitive IRPS or IR-DFWM measurements. Two detectors (the same type) were tested with the same PA-9 amplifier. The results are shown in Figure 3-6. Different background levels exist, which should be considered when using these infrared detectors for weak infrared signal collections.

3.3.2 Santa Barbara Focal Plane

Santa Barbara Focalplane, SBF-134, was employed for the work of infrared

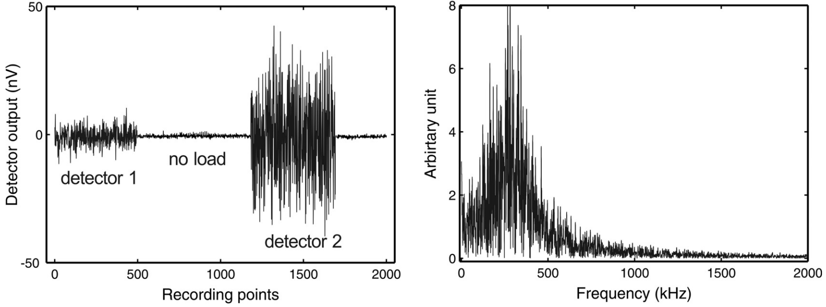

***Figure 3-6** (left): the background noise for two InSb detectors available in our lab. (right): Fourier transform of the noise recorded using detector 1. The detector only responses to the signals below 600 kHz owing to the PA-9 amplifier.*

imaging by IRPS, as described in *Paper* VIII. The sensor of this camera is InSb, also cooled by liquid N_2. The infrared camera has a 256×256 array size and a spectral response range between 1.0 - 5.2 µm. A liquid N_2 cooled filter mount is available for setting up different band-pass infrared filters. The infrared camera can be externally triggered, ensuring synchronization with the laser pulse.

3.4 Laboratory burners

Experimental work has been performed in flames produced on different burners that were chosen according to different research aims. Two burners often used in experiments as well as the typical characteristics of the produced flames are described below.

The porous plug burner

Premixed flat flames are suitable for studying species formation and consumption during combustion since these flames are quasi one-dimensional, showing varying properties as a function of height above the burner (HAB) in the central part. A typical McKenna burner and a home-built McKenna type burner were always used in the measurements.

Figure 3-7(a) shows an ethylene/air flame with an equivalence ratio of 2.0 burning on a McKenna burner [15]. The flow of mixed fuel and oxidizer is led through a centre plug (60 mm in diameter and water-cooled) made of stainless steel to produce a flat flame. In the outer plug, an annular co-flow of N_2 is used as a shielding layer to protect the inner flame from air movement in the laboratory. The flame is stabilized by a steel cylinder (also 60 mm in diameter) mounted 21 mm above the burner surface.

The McKenna burner is widely used as calibration source in different laboratories and is well studied for this purpose. In the current study, it was employed to produce sooty flames in which C_2H_2 measurement was performed using IRPS as in *Paper* IV. Figure 3-7(b) shows a lifted $CH_4/N_2O/N_2$ flame burning on a home-built McKenna type burner. The centre plug of this burner is 70 mm in diameter and specially arranged to be 2 mm above the outer annular plug to ensure close access of the laser beam to the burner surface. The flame shown in Figure 3-7(b) allowed measurements to be taken below the reaction zone.

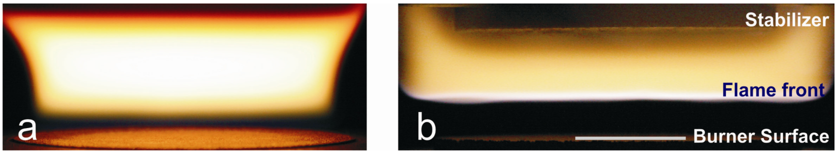

***Figure** 3-7 Flames produced on porous plug burners. **(a)** a C_2H_4/air sooty flame with the equivalence ratio of 2.0; **(b)** a lifted laminar $CH_4/N_2O/N_2$ flame.*

However, at atmospheric pressure, the sharp temperature gradient causes beam steering effects in coherent techniques like IRPS and IR-DFWM. Therefore, this McKenna type burner is often used in a low pressure chamber to address this issue, and to enlarge the reaction zone for space resolved measurements.

The Multi-jet burner

A multi-jet burner is designed to provide a laminar gas flow with temperature variable from 1000 K to ~ 2000 K. The burner consists of two main parts: jets and co-flow. In total there are 91 jets for burning CH_4/O_2/air mixed gas and every jet is surrounded by six small holes for N_2 co-flow. By changing the mass of co-flow gas, a gaseous environment with temperature ranging from 1000 K to 2000 K can be achieved in the post-flame region. A shielding ring is placed at a height of 2 cm on the top of the burner to ensure a sufficiently long distance for mixing between burnt gases and N_2 co-flow and to shield the mixed gas from the ambient air. A round (60 mm in diameter) stainless steel plate is placed 2 cm above the shielding ring to further stabilize the hot mixed gas flow. The schematic structure and photographs of the burner are shown in *Paper* IX. This burner was used in the work of *Papers* IX and VI.

In addition, a 2 mm diameter gas-welding torch was employed to produce a small cone-structure flame to test the spatial resolved ability of the techniques. In *Paper* VIII, this burner was used to demonstrate the imaging ability of IRPS.

Chapter 4

Infrared polarization spectroscopy (IRPS)

Polarization spectroscopy (PS) is a highly sensitive non-linear laser technique. It was firstly demonstrated by Wieman and Hänsch as a sensitive sub-Doppler spectroscopic technique for studying the hydrogen Balmer-β line and identifying the fine-structure components in the spectra [16]. It was introduced to flame studies in 1983 by Ernst [17] to measure intermediates BaO and CaCl, but limited to spectral studies. In 1985, Tong and Yeung applied PS to sodium and barium in flames for elemental analysis [18].

One year later, Zizak *et al.* demonstrated the detection of Na by PS using a pulsed dye laser [19], and from this publication PS began to be recognized as a promising technique in the area of combustion diagnostics. Since then, through one- or two-photon excitation, many species have been detected by PS, including C_2 [20], OH [21-25], CO [26], NH_3 [26], NH [24, 27], H [28-32], N_2 (1.2 - 5 bar at 300K) [33] and NO [25, 34]. PS also works in the infrared. By probing molecular ro-vibrational transitions, Li *et al.* measured combustion major products like H_2O and CO_2 [12], and fuel molecules like CH_4 [35], C_2H_2 [36] and C_2H_6 [37], even radicals CH_3 and OH [38]. Moreover, a number of researchers used picosecond laser in PS measurements to investigate intra-molecular relaxation rate [39] or collision rates [23, 40, 41]. However, it is still rare to find picosecond PS designed for diagnostics purpose.

Normally, PS works as a point-measurement tool. It can also be modified for two-dimensional imaging [21, 42, 43]. Temperature mapping was also achieved by probing two molecular level populations using the Boltzmann law [34, 44, 45].

Generally, PS is a pump-probe type coherent technique, which involves a linearly polarized probe beam interacting with the medium of interest between two axis-crossed polarizers and a stronger pump beam which is usually circularly or linearly polarized (45° rotated to the probe beam polarization). The probe beam is

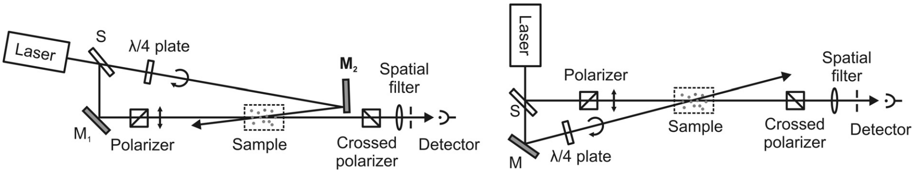

***Figure 4-1** A schematic PS set-up. The counter-propagating geometry is shown to the left for sub-Doppler high-resolution spectroscopy studies; and the co-propagating geometry, employed in IRPS, is shown to the right. (M, mirror; S, beam splitter).*

crossed with the pump beam at a small angle, defining the probe volume. Due to the anisotropy induced by the pump beam through resonant absorption from a molecular transition of the interrogated medium, the probe beam becomes slightly elliptically polarized, and consequently part of the probe beam leaks through the analyzer, forming the PS signal.

Usually two different pumping geometries are used in a PS set-up, counter- or co-propagating, as shown in Figure 4-1. The counter-propagating approach enables sub-Doppler detection, which was originally designed by Wieman and Hänsch for high-resolution spectroscopic investigations [16]. The co-propagating approach provides a stronger signal, resulting in a higher sensitivity. Therefore, the co-propagating geometry is employed in our mid-infrared PS for combustion diagnostics.

By using and developing IRPS, HCl measurements were performed in a laminar flame (*Paper* I) and in a smoke-laden furnace tube (*Paper* VII); HCN was quantitatively measured in $CH_4/N_2O/N_2$ flames (*Paper* V); C_2H_2 concentration was investigated in a sooty flame (*Paper* IV). Moreover, the potential of IRPS in heavily particle-laden environment was studied in *Paper* IX expanding the application of IRPS to aerosol, biomass and coal combustion.

4.1 Basic principle

The theory of polarizations spectroscopy can be found in the original papers of Hänsch *et al.* [16, 46] and in the textbook *Laser Spectroscopy* by Demtröder [47]. A short summary of the theory is given below.

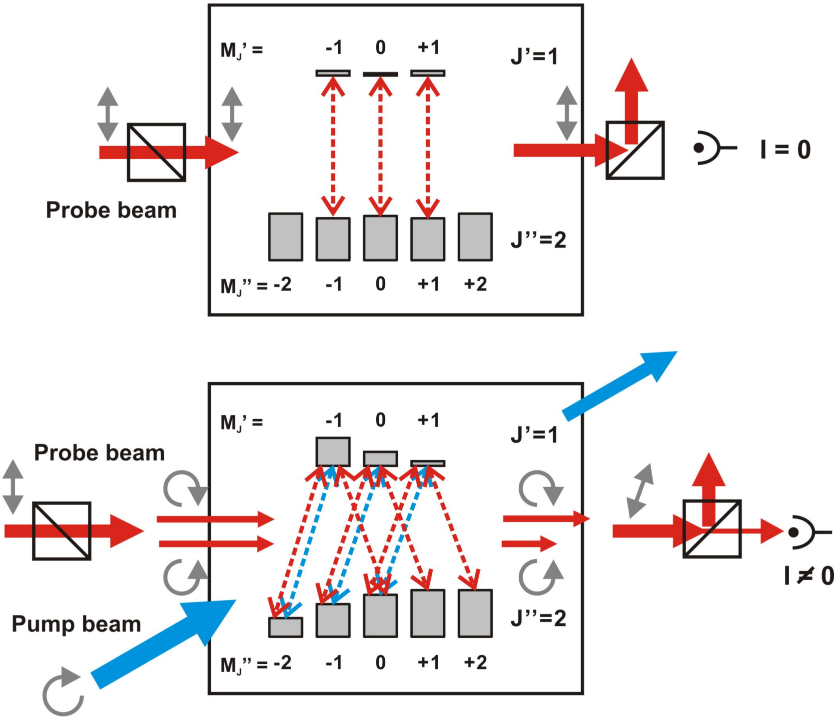

Figure 4-2 *Illustration of the PS signal generation process taking a P transition (ΔJ=-1) as example. Upper: without the pump beam, the linear polarization of the probe beam (in red) does not change during passing the sample, while only absorption happens. Lower: the circularly polarized pump beam (in blue) induces a non-uniform population among the magnetic sub-levels, equivalent to an anisotropic distribution of the angular momentum vector* ***J****. The sample becomes dichroic. The linearly polarized probe beam can be seen as consisting of a right- and a left-hand circularly polarized beams that have different absorption effect. Therefore the polarization of the probe beam is changed and the PS signal appears on the detector.*

Tuning the laser wavelength to an allowed transition (*J*' ← *J*"), the laser beam will be absorbed and the atoms or molecules will become excited. Depending on the polarization of the laser beam (the pump beam), however, only certain M_J sublevels (*J*', M_J') can be excited. ΔM_J equals +1 and -1, for right- and left-hand circularly polarized excited light, respectively. And $\Delta M_J = 0$ for linearly polarized excited light.

Figure 4-2 illustrates the generation process of the PS signal in a P transition (*J*' = 1 ← *J*" = 2) as an example. Without the pump beam, the probe beam is only attenuated due to sample absorption, and will be fully blocked by the second

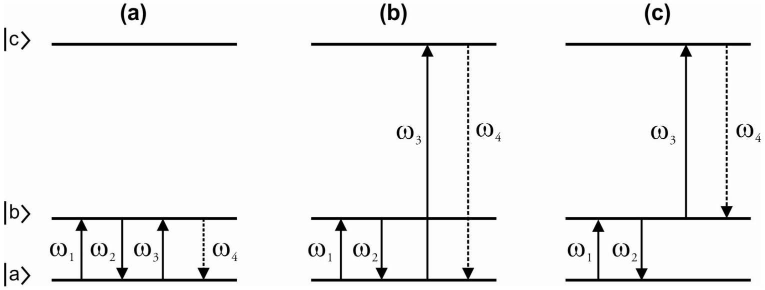

Figure 4-3 Energy level diagrams for polarization spectroscopy. (a) Degenerate PS that is used in this thesis; Double resonance (or two-color) PS that uses the induced anisotropy of lower state (b) and the upper state (c). $\omega_1 = \omega_2$ *works as the pump beam while* ω_3 *is the probe beam to produce the signal* ω_4.

polarizer. The right-circularly polarized pump beam induces a non-uniform population among the sub-levels, equivalent to an anisotropic distribution of the angular momentum vector $\boldsymbol{J}$. The sample becomes dichroic. The linearly polarized probe beam can be considered as the sum of a left- and a right-hand circularly polarized beam with equal intensity. These two parts are attenuated differently by the dichroic sample. In the case shown in Figure 4-2, the left-hand polarized component experiences stronger absorption; as a consequence, the polarization of the probe beam is rotated. This rotation is analyzed by the second polarizer, and the PS signal is generated.

It is not necessary to use the same frequency for the probe and pump beams, or to use the induced anisotropy in the lower state to generate the PS signal. As shown in Figure 4-3, besides of the typical scheme (a) the other two schemes (b) and (c) are also adopted in species detection. For example, scheme (b) was adopted for CH_3 radical measurements using infrared-ultraviolet double resonance [48] and scheme (c) was adopted for OH [49]. Sometimes, in schemes (b) and (c) the pumping process can be achieved using two- or multi-photon excitation [30, 32, 43]. However, in most cases, both pump and probe beams are produced from a single laser by a beam splitter for the simplicity of the experimental set-up. The model of the polarization signal in the unsaturated or the weakly saturated pumped condition was derived in [19, 46, 47] by ignoring the repopulation and de-phasing of the ground state due to collision and fluorescence. The derivation of Teets *et al.* [46] is used to demonstrate the PS theory.

The linearly polarized probe wave can be described as composed of two circularly polarized parts, σ^+ and σ^-, with the same phase and equal intensity. While passing through the excited sample induced by the pump beam, these two parts experience different absorption coefficients (α^+ and α^-) and different refraction indices (n^+ and n^-). Assuming the length of the beam crossed volume is l, the transmitted amplitude along the polarization of the second polarizer can be expressed as

$$E_t = E_0[\theta + ib + \frac{1}{2}(n^+ - n^-)\frac{\omega}{c}l + \frac{i}{4}(a^+ - a^-)l] \tag{4.1}$$

where E_0 is the probe amplitude; b is the extra ellipticity due to background birefringence like that from optical windows; ω is the light frequency; $(\pi/2-\theta)$ is the angle between the two polarizers. Note that it is assumed that the saturation is small, i.e. (n^+-n^-) and $(\alpha^+-\alpha^-) << 1$, and that the absorption is also small. For monochromatic light, the spectral absorption profile $\Delta\alpha(\omega)$ is Lorentzian and can be expressed as

$$\Delta\ a(\omega) = (a^+ - a^-) = \Delta\ a_0(\frac{1}{1+x^2}) \tag{4.2}$$

$$\text{with } x \equiv \frac{\omega_0 - \omega}{\gamma} \quad \text{and} \quad \Delta\ a_0 = \Delta\ a(\omega_0)$$

where $(\omega_0 - \omega)$ represents the detuning from resonance, and γ is the half width at half maximum (HWHM) of the absorption. In this case, the *Kramers-Kronig* relation gives a related dispersion-shaped curve for the refractive indices

$$\Delta n = (n^+ - n^-) = -\frac{1}{2}(\frac{c}{\omega})\Delta\ a_0 \frac{x}{1+x^2} \tag{4.3}$$

The transmitted intensity $I_t(\omega)$ at frequency ω reaching the detector is given by

$$\begin{aligned} I_t(\omega) = I_0(\omega)\{\xi + \theta^2 + b^2 - \frac{1}{2}\theta \cdot l \cdot \Delta\ a_0 \cdot \frac{x}{1+x^2} + \\ + \frac{1}{2} b \cdot l \cdot \Delta\ a_0 \cdot \frac{1}{1+x^2} + (\frac{1}{4}\Delta\ a_0 \cdot l)^2 \cdot \frac{1}{1+x^2}\} \end{aligned} \tag{4.4}$$

where the factor ξ (~10^{-6}-10^{-8}) is the extinction coefficient of the employed polarizers that takes into account the residual transmission of light. The signal induces a constant background term $\xi + \theta^2 + b^2$. For the PS set-up adopted in the current study, θ was always set to zero and was always avoided in order to prevent the introduction of any windows between two polarizers, i.e. $b = 0$. Therefore Eq. (4.4) can be simplified to

$$I_t(\omega) = I_0(\omega)\{\xi + \frac{1}{16} \cdot l^2 \cdot \left(\Delta\, \alpha_0\right)^2 \frac{1}{1+x^2}\} \tag{4.5}$$

The simplified relationship of Eq. (4.5) is also valid when a linearly polarized pump beam is employed under the same conditions. The major difference between the linearly polarized and the circularly polarized pump is the $\Delta\alpha_0$ term, i.e. the optical anisotropy related to the absorption cross section.

The absorption cross section (*M* dependence, i.e. $\sigma_{JJ'M}$) depends on the molecular total angular momentum *J*, the component *M* along the quantization axis, and the change of the total angular momentum *ΔJ* which has been interpreted in reference [46] and demonstrated in Figure 2 therein. $\sigma_{JJ';M}$ can be expressed based on the *Wigner-Eckart* theorem

$$\sigma^{\pm}_{JJ_1M} = \left\|\sigma_{JJ_1}\right\| \cdot C(J, J_1, M, M_1) \tag{4.6}$$

Here *J* and J_1 are the total angular momenta of the lower and upper state, respectively; $\left\|\sigma_{JJ_1}\right\|$ is a constant independent of *M*; $C(J, J_1, M, M_1)$ is the *Clebsch-Gordan* coefficients; and the plus and minus signs refer to right and left circular polarization, respectively. The total cross section σ_{JJ_1} can be defined by summing over *M*

$$\sigma_{JJ_1} = \frac{1}{2J+1} \sum_M \sigma^{\pm}_{JJ_1M} \tag{4.7}$$

Clearly, the cross section σ_{JJ_1} is independent of light polarization.

When considering the optical anisotropy. Time-dependent density-matrix equations solved by direct numerical integration (DNI) can be employed to calculate the optical anisotropy to simulate and interpret PS signals as shown in [50-53]. Another method for calculating optical anisotropy that could also be employed is the *diagrammatic perturbation theory* [54, 55]. For simplicity, optical anisotropy is calculated here using a more direct-forward approach based on rate equations.

Firstly, assume a simple model in which: (1) the pulsed laser duration *t* is small compared to the ground state relaxation time $1/\gamma_0$; (2) the pump and probe beam transition share a common lower level, but the upper state can be different; (3) the upper state does not contribute to the induced optical anisotropy (weak saturation); and (4) the molecule is at rest and is isolated, i.e. there is no any buffering molecule. For such a *perfect* condition, the pump laser depletes the population of the various Zeeman levels as

$$n_M = \frac{1}{2J+1} N_0 [1 - \sigma^{+}_{JJ_1M} \frac{I_{pump} \cdot t}{\hbar\, \omega_p}] \tag{4.8}$$

where n_M is the population in the M^{th} Zeeman level after pumping using a right circularly (+) polarized laser; N_0 is the total number density in the lower state; I_{pump} is the intensity of the pumping laser and t is its duration; J and J_1 are the total angular momenta of the lower and upper state, respectively. Then the absorption difference is

$$\Delta\, \alpha(\omega_{probe}) = (\alpha^{+} - \alpha^{-}) = \sum_{M} n_M (\sigma^{+}_{JJ_2M} - \sigma^{-}_{JJ_2M}) \tag{4.9}$$

J_2 refers to the total angular momentum of the upper state of the probed transition. Combining (4.6)-(4.9), we can get

$$\Delta\, \alpha(\omega_{probe}) = (\alpha^{+} - \alpha^{-}) = -(N_0 \sigma_{JJ_2}) \cdot (\sigma_{JJ_1} \frac{I_{pump} \cdot t}{\hbar\, \omega_{pump}}) \cdot \zeta_{JJ_1J_2} \tag{4.10}$$

In Eq. (4.10) the part of $N_0 \sigma_{JJ_2}$ represents normal absorption without the pump beam and hereafter expressed as $-\alpha(w_{probe})$. The numerical factor $\zeta_{JJ_1J_2}$, newly introduced, gives the J dependence of the polarization signals for the right circularly polarized pump, and its explicit expression of depending on J, J_1, and J_2 can be found in reference [46]. By defining a saturation parameter (**not** equal to the experimental saturation intensity, I_{sat}) as

$$S \equiv {}^{\hbar\, \omega_{pump}} \big/ {}_{t\, \sigma_{JJ_1}} \tag{4.11}$$

we have

$$\Delta\, \alpha(\omega_{probe}) = \alpha^{+} - \alpha^{-} = -\alpha(\omega_{probe}) \cdot (\frac{I_{pump}}{S}) \cdot \zeta_{JJ_1J_2} \tag{4.12}$$

Therefore, Eq (4.5) becomes

$$I_{PS}(\omega_{probe}) \cong I_{porbe}(\omega) \{\xi + \frac{1}{16 \cdot S^2} \cdot l^2 \cdot N_0{}^2 \cdot \sigma^2_{JJ_2} \cdot I^2_{pump} \cdot \zeta^2_{JJ_1J_2} \cdot \frac{1}{1+x^2}\} \tag{4.13}$$

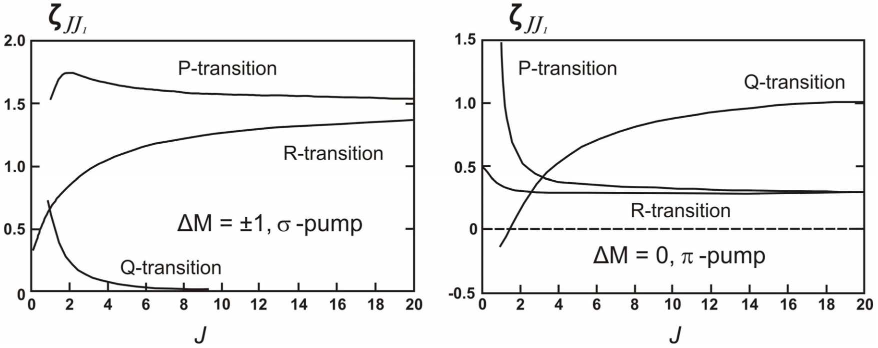

Figure 4-4 *The factor $\zeta_{JJ'}$ as a function of J values for (left) circular and (right) linear pump polarization. (from [47]).*

Some comments on Eq. (4.13) can be made:

1) $I_{PS} \propto (N_0)^2$, which is the basic relation for concentration measurement.

2) For the relatively large *J* values (*J* > 10), the factor ζ can find simple *ΔJ* dependence. For *ΔJ* = ±1 (P- and R-branches), the factor approach 3/2, while for *ΔJ* = 0 the factor decrease quickly to zero (*J* > 5), i.e. transitions of Q-branch exhibit less optical anisotropy when the circularly polarized pump beam is applied. (see Figure 4.3)

3) When $\theta = 0$, the maximum S/N ratio for PS signal is inversely proportional to the extinction coefficient, ξ, i.e.

$$\left(\frac{S}{N}\right)_{\max} \propto \frac{1}{\xi}$$

For this reason it is desirable to use very good polarizers in a PS set-up.

4) The discussion above assumes a circularly polarized beam as the pumping source. The condition in the case of a linearly polarized pump beam is similar. In particular the relation as shown by Eq. (4.13) is still valid. Specifically, a linearly polarized pumping geometry favors the Q-branch lines (see Figure 4-4).

4.2 Numerical modeling of PS

The discussions in the previous section are based on a much simplified model, in which the molecules are assume to be at rest and isolated. However, the actual condition of the molecules is much more complicated because they are in reality located in a collisional environment. The levels not coupled by the resonant pumping may in fact be strongly coupled to the pumped levels through different kinds of energy transfers (ET) processes, including rotational and vibrational energy transfer. Detailed numerical methods are required for a proper interpretation of the experimental PS signal.

Lucht and co-workers used the numerical solution of time-dependent density matrix equations by direct numerical integration (DNI) to investigate the line shape and saturation effects of the signals [50]. They also investigated the effects of a multi-axial-mode laser [51] and short-pulsed (picosecond) laser [56], the dependence of the signal on pump intensity and collision rate in the partially saturated regime [52]. In addition they looked at the effect of Doppler broadening [50, 56], and the dynamics of the moments of angular momentum distribution [53]. Only a very brief introduction to this extensive modeling is given here.

A schematic diagram of the energy-level structure incorporated in the DNI

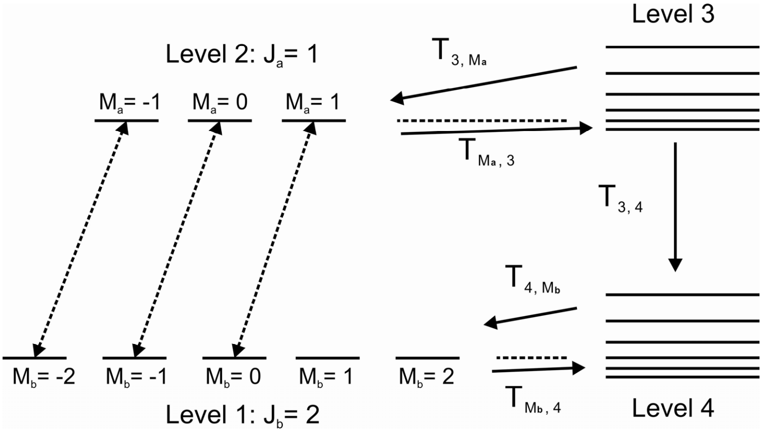

Figure 4-5 *Schematic diagram of the energy-level structure employed in the DNI calculations, taking a P(2) transition as an example. The dash lines with arrows indicate the coupling of the Zeeman states by the right circularly polarized pump beam. These coupling levels (1 and 2) are coupled to other rotational levels (bath levels, 3 and 4) in the upper vibration-rotation manifold and the lower vibration-rotation manifold, respectively. (from [50]).*

calculations is shown in Figure 4-5. The Zeeman levels related to PS signal generation are not only coupled to each other by the right circularly polarized pump beam, but are also strongly coupled to other ro-vibrational levels (bath levels, levels 3 and 4) by rotational transfer collisions with rates of $R_{3\text{-}Ma}$ and $R_{4\text{-}Mb}$. Both bath levels are also coupled with each other by electronic or vibrational quenching with a rate of $R_{3\text{-}4}$. The time-dependent density matrix equations for such a multistate system are [50]

$$\frac{\partial \rho_{kk}(\vec{r},t)}{\partial t} = -\frac{i}{\hbar}\sum_{m}(V_{km}\rho_{mk} - \rho_{km}V_{mk}) - R_k\rho_{kk} + \sum_{m} R_{mk}\rho_{mm} \tag{4.14}$$

$$\frac{\partial \rho_{kj}(\vec{r},t)}{\partial t} = -\rho_{kj}(i\,\omega_{kj} + \gamma_{kj}) - \frac{i}{\hbar}\sum_{m}(V_{km}\rho_{mj} - \rho_{km}V_{mj}) \tag{4.15}$$

where the diagonal matrix element ρ_{kk} is proportional to the population of level k; the off-diagonal matrix element ρ_{kj} describe the coherence between levels k and j; R_{mk} is the population transfer rate (in s^{-1}) from level m to level k; ω_{kj} is the angular frequency of the resonance between levels k and j; γ_{kj} is the dephasing rate of the coherence between levels k and j. $\gamma_{kj} = (R_k + R_j)/2 + \gamma'_{kj}$, where γ'_{kj} is the pure dephasing rate and R_k and R_j are population decay rates of levels k and j. The interaction operator V is given as

$$V_{km} = -\vec{\mu}_{km}\cdot\vec{E}(\vec{r},t) = -\vec{\mu}_{km}\cdot\left[\vec{E}_{probe}(\vec{r},t) + \vec{E}_{pump}(\vec{r},t)\right] \tag{4.16}$$

Under some assumptions and approximations, Eq.s (4.14-4.15) can be numerically solved by DNI. Details of this theory and the DNI model are not included here. Instead, only some important conclusions especially those which have been experimentally verified are provided here.

1) The use of picosecond laser pulses for PS holds obvious advantages in achieving quantitative diagnostics. In this case, when $\tau_L < \tau_C$ (τ_L, laser pulse width and τ_C, collision time), the collision rate dependence of the PS signal decreases significantly, even for nonsaturating pumping conditions. For saturating pumping conditions, the PS signal is nearly independent of collision rates. Increasing the collision rate from 10^8 to 10^{10} s^{-1}, the modeling results indicate that the PS signal only decrease by a factor of 2 for a 100 ps pumping laser pulse in the saturated regime [56].
2) Further direct numerical simulation by Lucht *et al.* [53] indicated thatfor the case of $\tau_L < \tau_C$ typically in a picosecond PS, probing a P-branch

transition in the unsaturated regime, the oriented anisotropy generated is mainly responsible for the PS signal using a circularly polarized pump beam. The alignment anisotropy that is generated, on the other hand, is largely responsible for the PS signal using a linearly polarized pump beam. In the saturated regime, the orientation and alignment make contributions comparable to the PS signal generation. For a Q-branch transition pumped by a circularly polarized beam, the contributions of the orientation and alignment are comparable. The strength of the PS signal can be enhanced by more than a factor of 20 for an initial oriented anisotropic distribution of the ground-state population achieved by a saturated pump beam, as compared to the isotropically distributed population.

3) Including the effect of the Doppler broadening and assuming a laser pulse of 3.5 ns (FWHM) in a counter-propagating geometry (Figure 4-1), the modeling results show that saturated PS favors quantitative concentration measurements [50]. As the transition nears saturation condition, the dependence of the signal strength on laser intensity and on the collision rate decreases drastically. In the low laser power (unsaturated) regime, the line-center PS signal is proportional to γ^{-6} (γ is collision rate) and in the near saturation regime, it is approximately proportional to γ^{-2}. The signal dependence on the collision rate is smaller for the line-integrated PS signal than for the line-center PS signal.

4) In terms of line shape, the simulated results show that at low laser power the *homogeneously* (*collision broadening dominate, i.e.* $^{\Delta\omega_D}/_{\Delta\omega_C} = 0$) broadened PS line shape is Lorentzian-cubed [50, 52], which is different to the conclusion of Lorentzian as shown in Eq. (4.13). The low-power PS line shows a Lorentzian shape when the *Doppler-* and the *collsion-* part are comparable. The line shape is close to pure Lorentzian in the strongly saturated regime [52].

5) When *Doppler broaden*ing is dominating, the intensity of the PS signal produced by a monochromatic laser varies with the Doppler and collisional widths, as does laser power, as follows:

$$I_{signal,unsaturating} \propto I_{probe} I_{pump}^2 \left(\frac{1}{\Delta\omega_D}\right)^2 \left(\frac{1}{\Delta\omega_C}\right)^4 \tag{4.17}$$

and

$$I_{signal,saturating} \propto I_{probe} \left(\frac{1}{\Delta\omega_D}\right)^2 \left(\frac{1}{\Delta\omega_C}\right)^{<1} \tag{4.18}$$

The fluctuation of the PS signal is much stronger when pumping is unsaturated rather than saturated, regarding the laser intensity fluctuations and collision effects. For absorption lines dominated by *homogenous broadening* especially under Doppler-free excitation, and with a neglected laser bandwidth ($\Delta\omega_L$ is small), a simple analytical expression was proposed by Walewski *et al.* [52]

$$I_{PS} = I_{probe} \cdot a \cdot \left(\frac{n \cdot I_{pump}}{I_{pump} + I_{sat}} \right)^2 \tag{4.19}$$

where a is a scaling factor, n is the number density of the probed species, and I_{sat} is the so-called PS saturation intensity. And

$$I_{ps} \propto \left(\frac{1}{\Delta\,\omega_C} \right)^3 \quad \text{for} \quad I_{pump} << I_{sat} \tag{4.20}$$

$$I_{ps} \propto \left(\frac{1}{\Delta\,\omega_C} \right)^1 \quad \text{for} \quad I_{pump} >> I_{sat} \tag{4.21}$$

The expression (4.19) can be extended to *inhomogeneous broadened* lines as

$$I_{PS} = I_{probe} \cdot a \cdot n^2 \cdot \frac{\left({I_{pump}}/{I_{sat}} \right)^2}{(1 + {I_{pump}}/{I_{sat}})^e} \tag{4.22}$$

with an extra empirical parameter, e.

6) The effect of using multimode laser radiation, i.e. a non-monochromatic laser source, on PS signal generation was studied by Reichardt *et al.* in [51]. The result can be summarized as: (1) When $\Delta\omega_L >> \Delta\omega_D$ for low pump power, the fluctuation of signal intensity from shot-to-shot is very high and the average signal level is much reduced as compared with the case of single-mode laser radiation. Increasing the pump power, the signal fluctuation decreases, and the ratio of pulse-averaged multimode signal to the single-mode signal increases. In the low pump power regime, the line width of the PS signal is narrower than the laser line width due to the non-linear nature of PS. (2) When $\Delta\omega_L << \Delta\omega_D$ (as in our IRPS experiments) for low pump power, the multimode signal level is actually enhanced, compared with the single-mode, owing to the intensity spiking in the

temporal profile. In the saturated pump power regime, the multimode signal level is near to that of the single-mode signal.

The generation of PS signal was, therefore, interpreted by achieving numerical solutions for time-dependent density matrix equations. On the other hand, the weak field PS signal was treated using a diagrammatic perturbative theory, resulting in an analytic solution. In the work of Reichardt *et al.* [54], a consistent conclusion for picosecond PS was found that the collisional dependence of the PS signal decreases significantly in the saturated regime. The analytical solution developed by Reichardt *et al.* was used to examine the effect of laser pulse duration on the collisional dependence of the PS signal in a weak field. Costen *et al.* used a diagrammatic perturbation theory to emphasize the significance of orientation and alignment tensor moments of the rotational angular momentum, as well as their collisional evolution [55]. The authors used a *Monte Carlo* integration to solve the derived equations.

It is important to note that the conclusions listed above were mainly derived based on counter-propagating PS geometry, and the modeling results were verified by PS measurements of the OH radical through its transitions in the UV. Special care is needed when applying these conclusions to the interpretation of IRPS signals because (1) Co-propagating geometry was employed in our IRPS study; (2) IRPS does not involve any electronic transitions and (3) the dominant line broadening effect is collision broadening rather than Doppler broadening as in the UV. The Doppler line width for C_2H_2 in flame temperatures is around 0.02 cm^{-1} at 3200 cm^{-1}, while the collision line width is around 0.05 cm^{-1} [57], and the laser line width was around 0.03 cm^{-1}.

4.3 Experimental set-up

A schematic view of a typical IRPS set-up is shown in Figure 4-6. The details of different components like the infrared laser, optics, polarizer, wave plates and InSb detector can be found in *Chapter 3*. For different individual IRPS experiments included in this thesis, small modifications were put in place. A co-propagating geometry was always used in our IRPS experiments.

The required mid-infrared laser from the laser system is rotated 90° to be vertically polarized by a half wave plate. A telescope consisting of two CaF_2 lenses (L1 and L2; f_1 = 500 mm and f_2 = -200 mm) is employed to produce a collimated beam. A HeNe laser beam is overlapped with the infrared beam through a diachronic mirror in order to allow visualization of the infrared beams and facilitate the optical alignments. Part of the laser beam is reflected by a beam splitter into a gas cell in order to monitor the laser frequency through the absorption spectrum of the selected gas (normally C_2H_2) filling the cell. Laser power fluctuation could also be monitored in this way. The laser beam transmitted through the beam splitter is focused by a lens (f_3 = 750 – 1000 mm) onto the measuring position (burner). The probe beam, a 7% reflection from the second CaF_2 beam splitter, is led through two crossed polarizers in between which only the burner is located. The entrance windows of both polarizers are adjusted to remain strictly perpendicular to the detection of the probe beam.

The transmitted part of the IR beam from the second beam splitter works as the pump beam. A tunable quarter-wave or half wave phase retardation plate is used to produce a circularly polarized or a 45° oriented linearly polarized pump beam. The probe beam and the pump beam are crossed at an angle of 3 – 6° geometrically defining the probe volume, which is approximately $0.3 \times 0.3 \times 8$ mm^3. PS signals leaking from the second polarizer are collimated by another CaF_2 lens (L4), which always has the same focal length as L3, before being sent to the

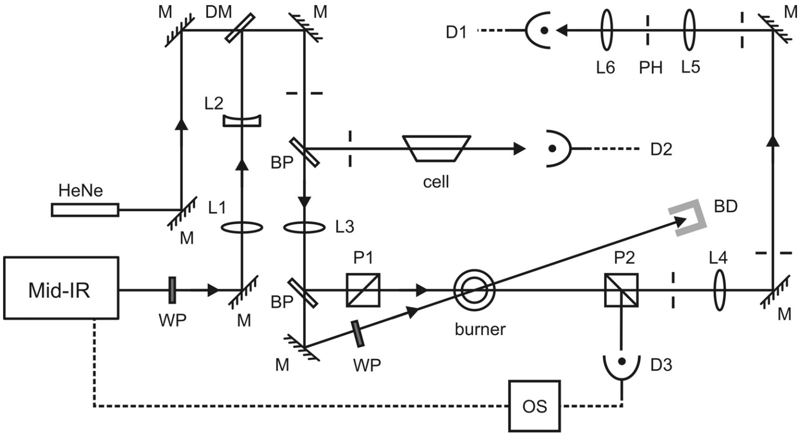

Figure 4-6 *Schematic diagram of the IRPS experimental arrangement. WP, tunable quarter-wave or half wave phase retardation plate; M, golden mirror; L, CaF_2 lens; DM, dichroic mirror; BP, Beam splitter (CaF_2 plate); P, YVO_4 polarizer; PH, pin-hole; D, InSb detector; BD, beam dump; OS, digital oscilloscope. Signals from D1 and D2 are also input to OS.*

InSb infrared detector (D1). A spatial filter consisting of two CaF_2 lenses and a pinhole is inserted in front of the detector to block spurious laser scattering. The reflected probe beam from the second polarizer is also measured by a detector (D3), through which the attenuation of the laser beam by the sample could be recorded, and used for detailed data processing (see *Papers* VII and IX). The transient signals from the IR detectors (D1, D2 and D3) are collected, time-integrated and stored in a 1 GHz bandwidth digital oscilloscope that is synchronized with the laser system.

4.4 Quantification of IRPS

Quantitative concentration measurement is still a challenging task in reacting flow diagnostics. In PS, for example, there are complex relations between the signal strength and experimental parameters, such as pressure, temperature, ambient species, detector sensitive, and collection efficiency. In such circumstances, online calibration is frequently adopted. During the current study of IRPS, a sample gas with a known concentration at room temperature (296 K) was always used to calibrate the IRPS signals measured in flames to get the concentration of the target species.

The IRPS line-integrated signal for the transition *J'* ← *J* in the saturate regime can be expressed by an empirical equation based on Eq.s (4.13) and (4.19)

$$I_{PS} = a \cdot I_{probe} \cdot g \cdot c \cdot \zeta_{JJ'}^{2} \cdot N_0^2 \cdot \sigma_{JJ'}^{2} \tag{4.23}$$

where a is a scaling factor; g is a parameter accounting for the spectral overlap between the laser line profile and the probed molecular absorption profile; c is a parameter accounting for the collision effects under different conditions (temperatures, pressures and buffer gases); the numerical factor $\zeta_{JJ'}$ gives the J dependence of the polarization signals; N_0 is the total number density in the lower state, and σ_{JJ_1} is the absorption cross section. At the gaseous temperature T, Eq. (4.23) can be rewritten as

$$I_{PS}(T) = a \cdot I_{probe} \cdot g(T) \cdot c(T) \cdot \zeta_{JJ'}^{2} \cdot \left\{ N(T) \cdot S_{JJ'}(T) \right\}^2 \tag{4.24}$$

where *N(T)* is the total molecule number in the probing volume, and $S_{JJ'}(T)$ is the line absorption intensity as in the HITRAN database. Note that the value of $S_{JJ'}(T)$ is extracted from the HITRAN/HITEMP database line-by-line.

If we performed measurement in flames and in calibration gases using the same IRPS set-up and probing the same transition, the parameters $\zeta_{JJ'}$, *a* and I_{probe} can be kept the same at flame temperatures and room temperature (296 K). By a simple derivation, the mole fraction of the investigated species in flames can be calibrated using information from the sample gas as follows

$$f(T) = f_{296} \cdot \frac{T}{296} \cdot \frac{S_{296}}{S_T} \cdot \left(\frac{g_{296}}{g_T}\right)^{\frac{1}{2}} \cdot \left(\frac{c_{296}}{c_T}\right)^{\frac{1}{2}} \cdot \left(\frac{I_T^{PS}}{I_{296}^{PS}}\right)^{\frac{1}{2}} \tag{4.25}$$

where *T* is the temperature in the flame. The effect of parameters *T*, *g* and *c* on the IRPS signal strength will be discussed in detail in the following subsections.

4.4.1 Temperature effect

In Eq. (4.25), the temperature *T* at the measuring point is critical. Indeed, the absorption cross section σ, the line overlapping factor *g* and the collision factor *c* are also functions of temperature. Temperature is needed to determine the values of σ, *g* and *c*, or their relative values at flame temperatures compared to room temperature. Moreover, one can notice that in Eq. (4.25) the mole fraction in flames *f(T)* is linearly proportional to *T*. It is also proportional to the square root of g_{296}/g_T and c_{296}/c_T, which indicates that the uncertainty of T_2 will results in a larger uncertainty in the final calculated mole fraction, *f(T)*, than the ratios of g_{296}/g_T and c_{296}/c_T.

As pointed out in *Paper* V, in which HCN quantitative measurements were performed in flames by probing the P20 line at 3248 cm^{-1}, a 5% temperature uncertainty resulted in around 20% uncertainty in the final mole fraction. Therefore, combining IRPS with other thermometry techniques, like CARS, is necessary to improve the accuracy and the precision of quantitative concentration results. Another option is to develop the application of IRPS in hot gas thermometry. By probing two lines, which have populations sensitive to temperature on the lower levels, provides intensity ratios that can reveal the flame temperatures. This idea has been demonstrated by the IR-DFWM of H_2O in our lab (*Paper* VI), and by the absorption spectroscopy of H_2O and CO_2 in Hanson group [58-62].

4.4.2 Spectral overlap

The absorption line width of molecular transitions in IRPS spectra narrows from room temperature to flame temperatures due to different collision rates and mean velocities at low and high temperatures. Therefore, the spectral overlap coefficient, *g*, for an excitation scan over an absorption line is consequentially a function of temperature. In general, the recorded line profile can be ascribed to the ensemble effects of collisional broadening (Lorentzian profile), Doppler broadening (Gaussian profile), power broadening and the laser line width, which is expressed as

$$L_{PS} = (L_{collision} \otimes L_{Doppler}) \otimes L_{laser} \tag{4.26}$$

It is always challenging to do a rigorous analysis, so the aim here is limited to evaluating the spectral overlap values. A global Voigt profile is used to characterize the molecular absorption profile. Characterizing the laser line shape by a Gaussian profile, with a width of 0.025 cm^{-1} (FWHM), the IRPS profile in the calibration gas and in flames are resolved by a de-convolution process, yielding the FWHMs of the global Voigt profiles in the calibration gas and in flames. The *g* coefficient is then determined by convoluting the laser line profile with the molecular absorption profiles fitted at the corresponding temperatures. Since the Doppler width can be calculated using the formula

$$\Delta \omega_D = \frac{2\omega_0}{c}\sqrt{\frac{2\ln 2 \cdot RT}{M}} \tag{4.27}$$

the collision width can be extracted by de-convolution of the global Voigt width with $\Delta\omega_D$. The collision width is narrower in flames than in gases at room temperature. The results from the current study showed that the *g* factor was enhanced about 2.1 times from room temperature to flame temperatures for HCN and C_2H_2. See *Papers* V and IV for details.

4.4.3 Collision effect

Temperature dependent collision effects are sophisticated and their inclusion in the quantification of PS measurements is challenging. A phenomenological approach is adopted in our work. The calibration gas is heated and the line-integrated IRPS signals are collected at different temperatures, as shown in Figure 4-7. The solid line is a polynomial fit for the measured value. The simulated signal intensities, without taking the collision-quenching effect into account, are shown as dots in

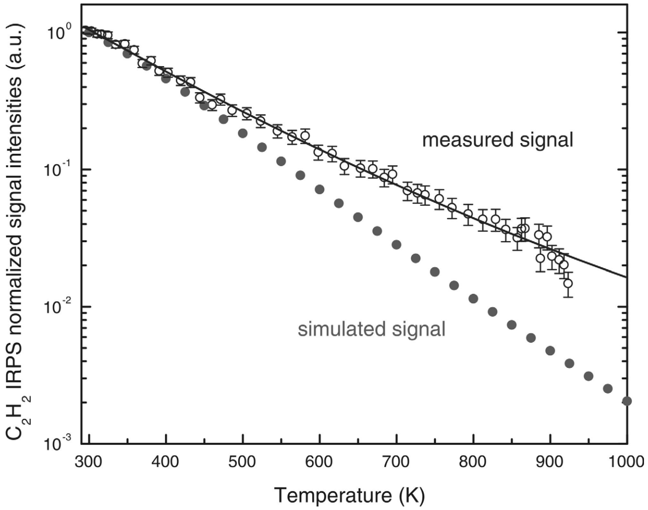

Figure 4-7 *The measured line-integrated IRPS signals (circles) of the C_2H_2 P13 line as a function of temperature. The dots show the simulation of IRPS signal intensity in a collision-free environment. The measured and simulated values are normalized at room temperature and the difference between them can be ascribed to the different collision effect at corresponding temperatures. The solid-line is a polynomial fit to the measured values in order to estimate the relative collision effects at higher temperatures.*

the figure. The simulated signals are normalized with the measured ones at room temperature. The difference between the measured and simulated values can be ascribed to the different collision effects (quenching and dephasing) at the corresponding temperatures. The calibration gas can hardly be heated above 950 K; there is therefore no measured value above this temperature. Instead, the polynomial fit of the presenting measured values is employed to estimate the collision effect in the high temperature range, up to flame temperatures around 2000 K.

Test results during the current investigation showed that in terms of quantitative measurements of HCN and C_2H_2 the *c* factor increased about 10 times from room temperature to flame (see *Papers* V and IV). In other words, the IRPS signals of HCN and C_2H_2 were enhanced about 10 times when subjected to flame temperatures due to the fact that the higher gas temperatures resulted in fewer collision. For an ideal gas with *Maxwell* distribution, the mean path and the average relative velocity appears approximately proportional to T and $T^{0.5}$, respectively. As a result, the average collision rate between gas molecules is proportional to $T^{-0.5}$. Fewer collisions occur at higher temperature; therefore, the IRPS signal is stronger at flame temperatures.

4.5 Applications

In this part, applications of IRPS for the detection of a few key species in particle-free and particle-laden flames are briefly introduced. The imaging capability of IRPS in flames is also demonstrated. The detailed descriptions of all these applications can be found in the attached papers. As mentioned previously, the PS signal is only generated from the crossing volume of the probe beam and the pump beams. Therefore, it can provide spatially resolved results, which is its great advantage compared with line-of-sight techniques. In the following subsections, it is shown that IRPS not only works for point-measurement but can also be used for two-dimensional imaging.

4.5.1 Applications in clean flames

Clean flames here refer to flames containing no soot or dust. In this thesis, HF, HCl and HCN have been investigated, for demonstrating the capacity of IRPS for quantitative concentration measurements. These three species have no electronic transitions suitable for combustion diagnostics. However, in the mid-infrared they have strong fundamental absorption bands due to the H stretching.

HCl detection was performed in the product zone of an atmospheric pressure premixed $CH_4/O_2/Ar$ flat flame produced on a McKenna type burner. Trace levels of HCl molecules were prepared by seeding a small amount of chloroform ($CHCl_3$) into the Ar flow. The spectral scanning range was from 3020 to 3090 cm^{-1}, where spectral interference from hot H_2O lines was relatively weak. Figure 4-8 shows two IRPS excitation scans, in which some OH lines can also be identified. Individual rotational lines from HCl and OH in the recorded IRPS spectrum were assigned and labelled in *C1*. Both $H^{35}Cl$ and $H^{37}Cl$ were identified. Scanning over the R(8) line, a detection limit of less than 50 ppm was estimated. The detail of this work is described in *Paper* I.

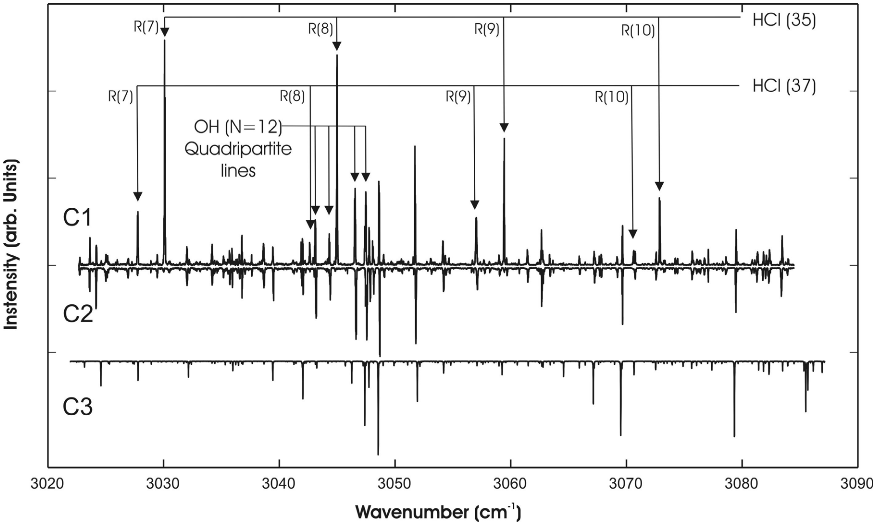

Figure 4-8 *IRPS excitation scans obtained in $CH_4/O_2/Ar$ flames with (C1) and without (C2) chloroform seeding. A simulated IRPS spectrum of water lines at 2000 K in the same spectral range is also shown (C3).*

Quantitative measurements of HCN molecules were performed in a series of lifted $CH_4/N_2O/O_2/N_2$ flames (see Figure 3-7). The flames were designed to be near-adiabatic, and the experimental results were compared with the modelling results by employing different detailed *nitrogen* chemistry mechanisms. The spectral range studied was 3200 – 3300 cm^{-1} and the P(20) line at 3248.5 cm^{-1} was chosen for concentration measurement mainly due to the weak spectral interference from H_2O lines. An on-line calibration was conducted during the measurements. In data evaluations, collision effects and the spectral overlap coefficient were considered. Generally, good agreement was found between measured and modelled results. It proved difficult however to use IRPS (and other coherent laser-based spectroscopic techniques) to conduct measurements in the flame front, where sharp temperature gradients exist and cause beam steering and dispersion effects. However, these effects can be greatly reduced in low pressure flames (for example 50 mbar) because of the low gas density. The details of this work are described in *Paper* V.

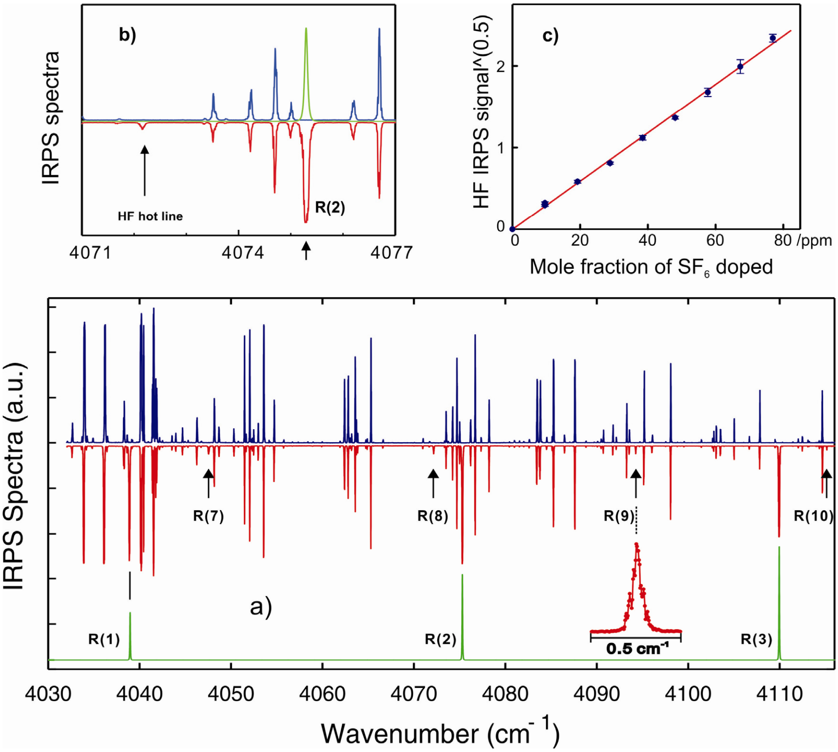

Figure 4-9 (a) *IRPS excitation scans in CH_4/air flames; (blue line) without and (red line) with SF_6 seeding and (green line) the simulated HF IRPS spectrum at 1800 K based on the HITRAN database. The rotational lines R(J) are assigned, where J = 1 to 3 for the (1-0) band and J = 7 to 10 for the (2-1) hot band. A zoom-in of the R(9) line of HF is shown for clearance. (b) the zoom-in of part of excitation scans for clearance.* ***(c)*** *linear relation between the square root of the HF IRPS signal intensity and the mount of SF_6 seeded into flames.*

HF detection was performed in premixed CH_4/air flames using a McKenna type burner. A small amount of SF_6 was seeded into the flames to produce HF molecules. This investigation involved the preparation of spectral information for HF imaging in flames using IRPS (discussed in *section 4.5.3*). As shown in Figure 4-9, the measured spectral range was 4030 – 4120 cm^{-1} (around 2.5 μm). This range avoided the interference of strong absorption bands of H_2O. HF lines from the (1-0) and (2-1) bands were assigned and labelled in the measured spectrum with the assistance of the HITRAN database.

The dependence of the IRPS signal strength on the mount of seeded SF_6 was also studied. As shown in Figure 4-9(c), a good linear relation was obtained. Note here that the HF signals in Figure 4-9(c) had been corrected for the energy fluctuations of the probe beam. In the spectral range investigated here, HF lines are mostly free of spectral interference from H_2O, which is an obvious advantage for species detection using spectroscopic methods. The R(3) line of the (1-0) band and the R(9) line of the (2-1) band were excited for *cold* and *hot* HF imaging in a jet CH_4/O_2 flame (see *subsection 4.5.3*).

4.5.2 Sooty and particle-laden flames

Besides of *clean* flames, IRPS was also employed in sooty flames and particle-laden combustion environments. In *Paper* IV, quantitative measurement of C_2H_2 in a series of rich premixed C_2H_4/air flames (see Figure 3-7(a)) was described. It was found that even when the soot-volume fraction (SVF) is up to 2×10^{-7}, no obvious degrading of the IRPS technique appeared. The primary particle diameter was approximately 10 nm in the studied flames.

Even in harsher combustion environments, IRPS continued to perform effectively. In *Paper* VII, IRPS was used to investigate HCN and HCl production and consumption during the burning of polyvinyl chloride (PVC) carpet and Nylon 6.6 in a tube furnace 170 cm long. Along the tube, there was dense smoke and droplets that strongly scattered the trending HeNe laser beam, but the IRPS signal was still observable. IRPS measurements provided spatially resolved, in situ results in contrast to the most common probe methods following a FTIR (Fourier Transform Infrared) spectrometer at the end of a tube.

IRPS was also applied in aerosol- and coal/bio particle-laden combustion environments. In *Paper* IX, the effective use of IRPS in HCl measurement in a K_2SO_4 aerosol laden environment was demonstrated, where $2KCl + SO_3 + H_2O = K_2SO_4 + 2HCl$ occurs (see Figure 4-10), along with HCN measurements in biomass (wood) and coal combustion. IRPS showed an outstanding feature on tolerating the particle scattering. Besides of the experimental demonstrations, the background physics of particle scattering suppression in IRPS is discussed in *Paper* IX. Moreover, IRPS shows potential for quantitative measurement in harsh particle-laden environments.

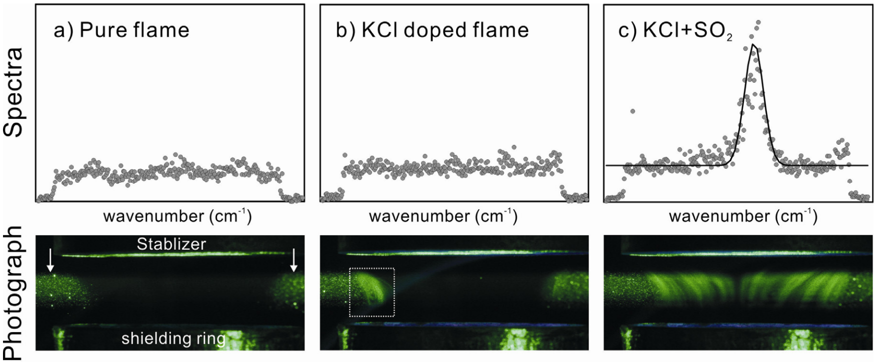

Figure 4-10 *(upper) The IRPS excitation scans and (lower) direct view of Mie scattering during HCl measurement in aerosol-laden environment. Mie scattering from ambient air is shown by arrows in* ***(a)****, and Mie scattering of KCl fog seeded into flame is shown in the dashed box in* ***(b)****. The measured HCl and corresponding Mie scattering from produced* K_2SO_4 *aerosol are shown in* ***(c)****.*

4.5.3 Two dimensional IRPS

In *Paper* VIII, two-dimensional (2D) imaging using the IRPS of hydrogen fluoride (HF) molecules was demonstrated in flames by exciting the R(3) line (see the spectra in Figure 4-9) belonging to the fundamental vibration band using a laser beam at 2.5 µm. Single-shot 2D images of the HF molecules were recorded in a premixed CH_4/O_2 jet flame seeded with a small amount of SF_6 (2%), as shown in Figure 4-11(d). An orthogonal geometry was adopted, with a laser sheet as the pump beams perpendicularly crossed with a collimated probe beam. This arrangement guaranteed a high spatial resolution. The spatial-resolved ability was checked by inserting a scaled plastic plate with a line width of 130 µm, and the image produced by the plastics plate birefringence is shown in Figure 4-11(a). A spatial resolution of around 100 µm was estimated. This work appears the attached *Paper* VIII, in which the details of the set-up, the polarization states of the probe and pump beams, and the image capturing system are described.

As a coherent technique, IRPS greatly suppresses the strong thermal background radiation from the flames; but, as shown in Figure 4-11(b), there was still residual thermal radiation collected by the IR camera even it was situated two meters away from the flame, with the polarizer and aperture blocking the radiation from the flame. Therefore, it is suggested that narrow band IR filters be employed after the second polarizer since that IRPS signal is as pure as the laser source in frequency while the flame radiation is much more broadband.

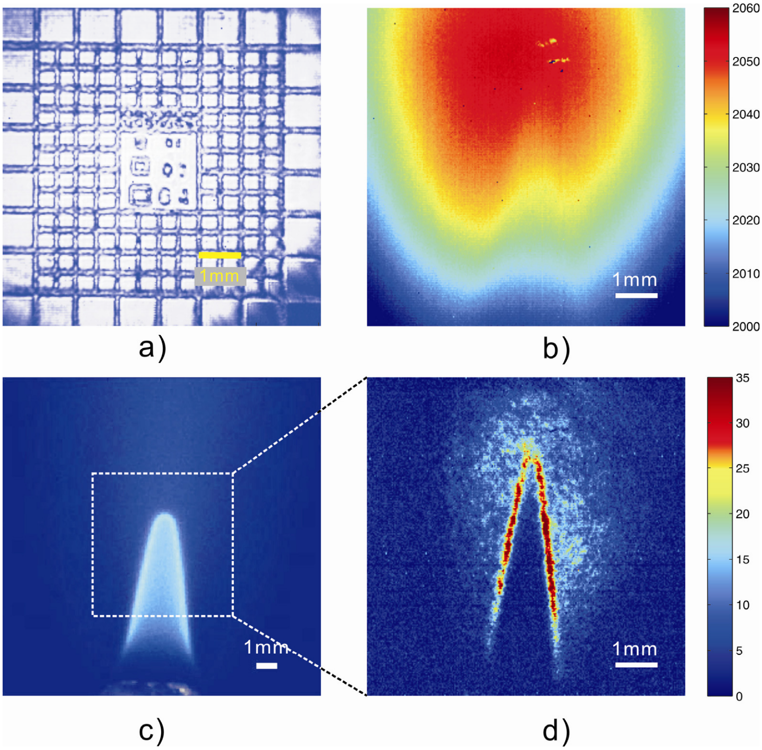

Figure 4-11 (a) the spatial resolved ability of the 2D-IRPS set-up was tested by inserting a scaled plastic plate with a line width of 130 μm. PS image was induced by the plastics plate birefringence. (b) the background signals composed of the dark current noise of the IR camera and the flame thermal emission, around 2000 and 60 counts (in arbitrary unit), respectively. (c) The direct view of a φ = 2.0 CH_4/O_2 jet flame seeded with 2% SF_6. (d) IRPS image of HF produced in the left flame by probing R(3) line of (1-0) band. The gate time of the IR camera was kept to 0.96 μs during the measurements.

Figure 4-11(c) and (d) show the direct view of the investigated cone-structure flame and the HF image using 2D-IRPS, respectively. Generally, the 2D-IRPS technique offers unique features, including high temporal and spatial resolution, interference free from background emission and good chemical selectivity. This makes it highly suitable for imaging different infrared-active molecular species, particularly in harsh environments, like flames and plasma. 2D-IRPS works as a complement for point-measuring IRPS that provides highly sensitive measurements.

4.5.4 Low pressure IRPS

The applications of IRPS in atmospheric pressure flames/combustions have been described in the three previous subsections. The applications of IRPS in low pressure flames for major or minor species measurements were also demonstrated in our group by *Li* [36, 38], where the two polarizers were located in the low pressure chamber to avoid the birefringence from the chamber optical windows.

Li's work was limited to qualitative measurements. Low pressure IRPS offers potential advantages in quantitative measurement as well. IRPS signal intensity depends strongly on collision effects, meaning different ambient temperature and different neighbouring species can influence IRPS signals. Accurate quantitative measurement using IRPS can, therefore, be difficult. When collision is lessened by a low pressure environment, however, IRPS can provide more accurate quantitative

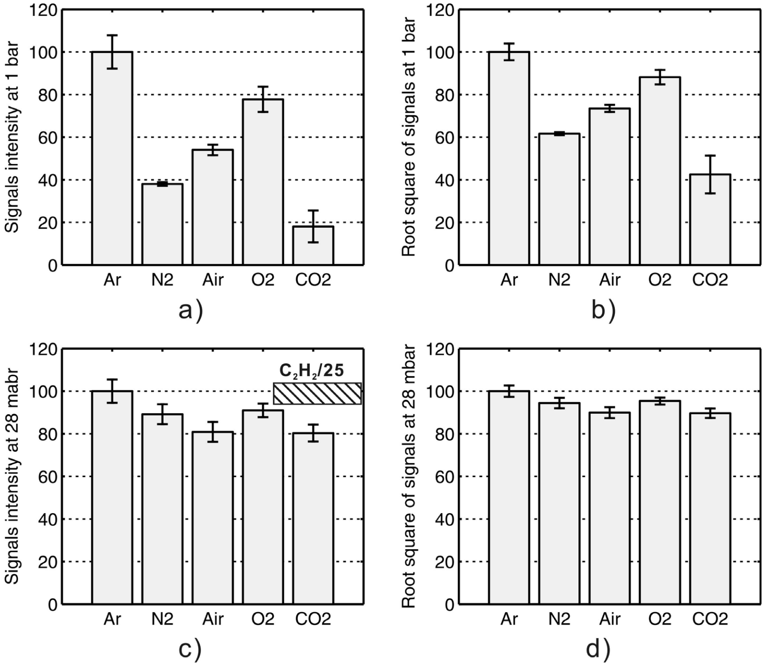

***Figure 4-12** Normalized IRPS signal intensities of C_2H_2 buffered with different gases **(a)** at atmospheric pressure and **(c)** at low pressure 28 mbar. The corresponding root squares of IRPS signal intensity are shown in **(b)** and **(d)**. In **(a)** the partial pressure of C_2H_2 is 0.5 mbar while in **(c)** its partial pressure is 0.015 mbar. Note that in **(c)** the diagonal striped box indicates the signal level, divided by 25, of 'pure' C_2H_2 (0.015 mbar C_2H_2 in 2.180 mbar grounding pressure), The thickness of the diagonal striped box indicates the uncertainty. All measurements were performed at 296 K.*

results. As shown in Figure 4-12(a), different buffering gases significantly influence the signal intensity at atmospheric pressure, resulting in a large uncertainty in concentration. But measurements at low pressure can give more accurate results because of less collision effect; see Figure 4-12(d). Moreover, low pressure can also reduce the *J*-dependence of the IRPS signal, which will increase the accuracy of IRPS thermometry applied in low pressure flames.

Chapter 5

Infrared degenerate four-wave mixing

Degenerate four-wave mixing (DFWM) was proposed for combustion diagnostics in 1982 by Ewart *et al.* [63] and was used to study phase-conjugation in flames in 1985 [64]. In these two works, atomic sodium was measured. The first combustion species studied by DFWM was OH in 1986 by Ewart *et al.* [65]. From that time, DFWM has been successfully applied for the detection of various transient and stable species in flames by resonantly probing strong electronic transitions, such as OH [65, 66], CH [67], NH [66, 68], CN [69], C_2 [70, 71], NO [14], NO_2 [72] and atomic oxygen [73]. The strong resonant enhancement of the reflectivity of DFWM in absorbing gases is the basis of its sensitivity for the detection of minor species. Scanning a spectral range covering several rotational lines, gas temperature can be derived by fitting the measured spectrum with the simulation [74]. Moreover, multiplex DFWM for thermometry application is also possible using broadband laser radiation to excite several lines [74-78], taking OH and C_2 as the target species. It is also possible to do imaging using DFWM by forming the pump beam to a thin laser sheet and using a collimated probe beam [79-81]. Infrared DFWM has also been developed to measure species having accessible absorption in the mid-infrared, such as CH_4 [82, 83], C_2H_2 [83] and C_2H_4 [84].

In ways similar to PS, experimental or theoretical work was conducted to investigate the dependence of DFWM signal strength on transition dipole moment [85], collision quenching [86], saturation effect [87-91], angular momentum *J* [92], Doppler broadening effects [93], short laser pulse (picosecond) [94], phase-matched geometry [95] and polarization effects [90, 96]. The theoretical investigations were performed using diagrammatic perturbation theory or direct numerical integration (DNI) of the time-dependent density matrix equations. Comprehensive reviews of DFWM spectroscopy and its diagnostics applications can be found in references [97-100].

In the work of this thesis, a stable set-up for IR-DFWM was developed to simplify the optical alignment. IR-DFWM can meet the need for diagnostics in a closed chamber, where the windows cause a birefringence to the PS technique and therefore a disturbing background level. In this chapter, a grating-picture of the DFWM is employed to interpret the generation of signals. General expressions of signal strength are adopted from literatures without any detailed derivations. The experimental set-up we developed for the current study and its application to thermometry are briefly introduced. A special four-wave mixing scheme with non-resonant pump and resonant probe in the UV/visible range for OH detection in flames is not included here, but is included as an attached paper (*Paper* II).

5.1 Basic principle of DFWM

The interaction of light with matter can be simply expressed as

$$P(\omega) = \varepsilon_0 \chi^{(1)}(\omega) E(\omega) \tag{5.1}$$

where $P(\omega)$ is the dipole moment per unit volume, or polarization; ε_0 is the permittivity of free space; $\chi^{(1)}(\omega)$ is known as the linear susceptibility and $E(\omega)$ is the electric field of the incoming light wave. The non-linear optical response can often be described by generalizing Eq. (5.1) by expressing the polarization as a power series in the electric field strength as in [101]

$$\begin{aligned} P(\omega) = \varepsilon_0 \chi^{(1)}(\omega) E(\omega) + \varepsilon_0 \chi^{(2)}(\omega) E^2(\omega) + \\ + \varepsilon_0 \chi^{(3)}(\omega) E^3(\omega) + \ldots \end{aligned} \tag{5.2}$$

The quantity $\chi^{(n)}(\omega)$ is the n^{th}-order non-linear optical susceptibility. Eq. (5.2) is also valid for polarization induced by more than one field with a different frequency. The four-wave mixing process is related to the third-order term of Eq. (5.2)

$$P_{fwm}(\omega_l) = \varepsilon_0 \chi^3_{ijkl} E_i\left(\omega_i\right) E_j\left(\omega_j\right) E_k\left(\omega_k\right) \tag{5.3}$$

This process can also be thought as the field $E_k(\omega_k)$ acting on the medium whose refractive index is being modified by the other two fields, $E_i(\omega_i)$ and $E_j(\omega_j)$

$$P_{fwm}(\omega_l) = \varepsilon_0 \left[\chi^3_{ijkl} E_i\left(\omega_i\right) E_j\left(\omega_j\right) \right] E_k\left(\omega_k\right) \tag{5.4}$$

The four electric fields satisfy the rules of energy and momentum conservation as

$$\omega_l = \omega_i \pm \omega_j \pm \omega_k \tag{5.5}$$

and $$\vec{k_l} = \vec{k_i} \pm \vec{k_j} \pm \vec{k_k} \tag{5.6}$$

Eq. (5.6) is also called the *phase matching* rule. In the case of DFWM, the three incoming waves have the same frequency, i.e.

$$\omega_4 = \omega_1 - \omega_1 + \omega_1 = \omega_1 \tag{5.7}$$

In some cases, two-color FWM (TC-FWM) is employed in combustion diagnostics, in which the relation between the frequencies of the waves is

$$\omega_4 = \omega_1 - \omega_1 + \omega_2 = \omega_2 \tag{5.8}$$

The molecular transitions involved in the DFWM process are shown in Figure 5-1(a) and two different geometrical arrangements satisfying the phase matching are shown in (b) and (c), namely the phase-conjugate geometry (PCG) and the forward phase-matched geometry (FPG). Two of the incident beams are designed as the *pump beams* and the third one is the *probe beam*. A spatially varying intensity pattern or grating is written into the resonant-absorption medium by the interference of the two pump beams. The scattering of the third beam by this grating forms the signal beam. A stationary population grating is formed by the degenerated pumping and the spacing of the grating Λ is dependent on the color of the laser beams λ_p and the crossing angle θ between them

$$\Lambda = \frac{\lambda_p}{2\sin(\theta/2)} \tag{5.9}$$

In principle, an arbitrary crossing angle can be used. However, in practice, a small angle θ is always used since a large angle results in a narrow spacing, and the grating can be washed out easily by the thermal motion of the molecules.

The energy in the excited molecules can be released as heat in the medium to form a thermal grating. The thermal grating can also reflect the third beam to contribute to the coherent signal, in particular in an environment with significant collisions, as take place at ambient and evaluated pressures [102-106]. Indeed, both the population grating and the thermal grating contribute to the DFWM signal. These two gratings, however, proceed on different timescales, and thermal grating influences the DFWM signal and complicates signal interpretation. Fortunately,

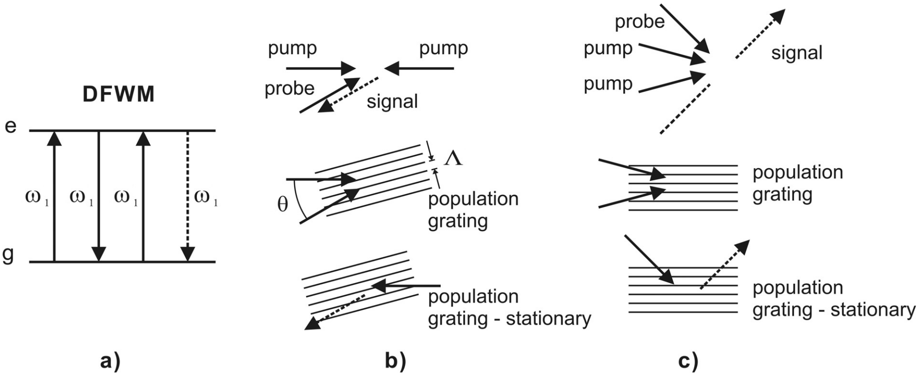

***Figure 5-1 (a)** Transitions between energy levels involved in DFWM. The three incoming waves of the same frequency are represented by the solid arrows while the signal beam emitted is shown by the dash arrow. Grating pictures to interpret the generation of DFWM signals in two geometries **(b)** the phase-conjugate geometry, PCG, and **(c)** the forward phase-matched geometry, FPG. Two of incident beams construct a stationary population (excited) grating which can reflect the third beam to generate the signal beam.*

the signal strength is dependent on the square of species concentration in both the population grating and thermal grating process. Therefore, the two types of signal source do not need to be distinguished when DFWM is used for concentration measurement. Moreover, in the mid-infrared DFWM, the issue of thermal grating is essentially unimportant because the laser pulse duration is approximately 4 ns. On such a timescale, thermal grating cannot be built since the excitation energy absorbed by the molecules needs time to release into the surrounding and elicit thermalization [104].

The currently most accepted theory of DFWM in a two-level absorbing system in the general case was published by Abrams and Lind in 1987. They worked out a quantitative description of amplified reflection, oscillation and phase conjugate [107]. Although the A&L model involved some simplifications, it continues to successfully predict the behavior of DFWM in a wide range of situations. Assuming that absorption of the two equal pump beams is negligible and allowing for absorption of the probe beam and the pump beam, a more readable expression of the DFWM signal in terms of atomic or molecular parameters was generated by [85]

$$I_{sig} \propto \frac{1}{\left(1+\delta^2\right)} \alpha_0^2 L^2 \frac{4(I_{pump}/I_{sat})^2}{(1+4\,I_{pump}/I_{sat})^3} I_{probe} \tag{5.10}$$

where $$\alpha_0 = \frac{\omega \cdot \Delta n \cdot \mu_{12}^2 \cdot T_2}{2\varepsilon_0 c\hbar} \tag{5.11}$$

and $$I_{sat} = \frac{\varepsilon_0 c\hbar^2}{2T_1T_2\mu_{12}^2}(1+\delta^2) = I_{sat}^0(1+\delta^2) \tag{5.12}$$

where α_0 is the unperturbed line-center field absorption coefficient; Δn is the population difference in the absence of an applied field; μ_{12} is the transition dipole moment, c is the light speed, ε_0 is the permittivity of vacuum, L is the interaction length, and δ is the detuning of the applied field and absorption transitions. Note that T_1 is the population decay time of the population excitation, also called the longitudinal relaxation time, and is determined by the radiative lifetime of the excited state. T_2 is the coherence decay time, also called transverse relaxation time, and is determined by the de-phasing rate of the dipole oscillations and usually determined by the collision rate. In the low- and high-intensity limits,

$$I_{sig} \propto \frac{1}{\left(1+\delta^2\right)}\alpha_0^2 L^2 \cdot 4(I_{pump}/I_{sat})^2 I_{probe} \propto \frac{\mu_{12}^8(\Delta n)^2 L^2 T_1^2 T_2^4}{\left(1+\delta^2\right)^3} I_{pump}^2 I_{probe}$$

for ($I_{pump} << I_{sat,\ \delta = 0}$) (5.13)

$$I_{sig} \propto \frac{1}{\left(1+\delta^2\right)}\alpha_0^2 L^2 \cdot (I_{sat}/16 I_{pump}) I_{probe} \propto \frac{\mu_{12}^2(\Delta n)^2 L^2 T_2}{T_1} I_{pump}^{-1} I_{probe}$$

for ($I_{pump} >> I_{sat,\ \delta = 0}$) (5.14)

The spectrally integrated DFWM signal is also used,

$$I_{sig}^{in} \propto \frac{3\pi}{2T_2}\alpha_0^2 L^2 \frac{4(I_{pump}/I_{sat}^0)^2}{(1+4I_{pump}/I_{sat}^0)^{5/2}} I_{probe} \tag{5.15}$$

and the low- and high-intensity limits of Eq. (5.15) are

$$I_{sig}^{in} \propto \frac{\alpha_0^2 L^2}{T_2} \cdot (I_{pump}/I_{sat}^0)^2 I_{probe} \propto \mu_{12}^8(\Delta n)^2 L^2 T_1^2 T_2^3 I_{pump}^2 I_{probe}$$

for ($I_{pump} << I_{sat,\ \delta = 0}$) (5.16)

$$I_{sig}^{in} \propto \frac{a_0^2 L^2}{T_2} \cdot (I_{sat}^0 / I_{pump})^{1/2} I_{probe} \propto \mu_{12}^3 (\Delta n)^2 L^2 T_1^{-1/2} T_2^{1/2} I_{pump}^{-1/2} I_{probe}$$

$$\text{for } (I_{pump} >> I_{sat,\ \delta = 0}) \qquad (5.17)$$

Eq.s (5.10)–(5.17) require further explanation in the context of the current study. Firstly, these equations were derived for *phase conjugate* geometry (PCG). Reichardt *et al.* theoretically compared the line shapes and signal intensity between two geometries (PCG and FPG, see Figure 5-1) using the DNI of the time-dependent density-matrix equations [95]. Their results indicated that FPG is less sensitive to the Doppler line width at low laser intensity. In the case of $I_{pump} \approx I_{sat}$, the signal for FPG is stronger than that for PCG for primarily Doppler-broadened resonances. According to Reichardt's work [95], in the case of $\Delta\omega_D/\Delta\omega_C = 0.5$ (a condition similar to the current study's mid-infrared DFWM) the signal for FPG is stronger than that for PCG in the range of $I_{pump}/I_{sat} \leq 10$.

Secondly, the line-integrated signals strength is less sensitive to collisions than the line central signal strength. Therefore the line-integrated signal is always used. One can see by comparing Eq. (5.16) and Eq. (5.17), that in the saturated regime the collisional influence is even less. That is to say, in the case of strong, or saturating, pump beams ($I_{pump}/I_{sat} \geq 1$) the collisional dependence is considerably weaker. Moreover, the use of saturating pump beams minimizes the effects of beam absorption, providing more-accurate concentration measurements [89]. It is important to note, however, that when $I_{pump}/I_{sat} >> 1$, the signal strength decreases with increases in pumping intensity. So in real measurement it is advisable to plot the signal strength as a function of pump intensity in order to choose a suitable pump intensity.

Thirdly, the signal strength keeps scaling with $(\Delta n)^2$, which is the basis for concentration measurements using DFWM. However, the complex dependence of the signal strength on the transition dipole moment μ_{12} causes difficulty in the fit of measured spectrum that varies with saturation degrees. Farrow *et al.* showed that saturated spectra analyzed by assuming a $\mu^4(\Delta n)^2$ signal dependence could yield temperatures that agreed well with the CARS measurements [85].

As pointed out by Ewart *et al.* [99, 100], in practical diagnostics we have to deal with (1) atomic or molecular motion; (2) laser pulse duration (τ_{laser}) and its non-monochromatic effect; (3) the effect of the strong probe field (like in our case); (4) optical thickness; (5) more complex collisions; and (6) level degeneracy and polarization effects. These challenges were one of the reasons for the development of theoretical methods, such as diagrammatic perturbation theory and

DNI of the time-dependent density matrix equations, to improve the A&L model. Research in this area has been summarized by Kiefer and Ewart [99, 100], and only two important points are mentioned here.

Reichardt *et al.* [93] calculated the line-center reflectivity using the DNI numerical approach and obtained a modified analytical expression as

$$R = \frac{R_{\text{hom}}}{1 + (b\Delta\,\omega_D / \Delta\,\omega_C)^2} \tag{5.18}$$

where R_{hom} is the homogenous reflectivity derived from the A&L model

$$R_{\text{hom}} = \frac{I_{sig}}{I_{probe}} \propto \frac{1}{1+\delta^2}\alpha_0^2 L^2 \frac{4(I_{pump}/I_{sat})^2}{(1+4I_{pump}/I_{sat})^3} \tag{5.19}$$

$\Delta\omega_D$ and $\Delta\omega_C$ are Doppler and collisional widths, respectively; b is an empirical parameter, weakly dependent on the pump and the probe powers. This modified reflectivity expression (5.18) proved to be valid over a wide range of values for the ratio of Doppler to collisional width. It should be noted, however, that this reflectivity expression was derived based on a phase-conjugate geometry DFWM. In another work [89], it was concluded that for a primarily Doppler-broadened environment, the DFWM signal produced by a monochromatic laser could be scaled as

$$I_{signal,unsaturating} \propto I_{probe} I_{pump}^2 \left(\frac{1}{\Delta\,\omega_D}\right)^2 \left(\frac{1}{\Delta\,\omega_C}\right)^4 \tag{5.20}$$

for unsaturated pumping and

$$I_{signal,unsaturating} \propto I_{pump}^{-1} I_{probe} \left(\frac{1}{\Delta\,\omega_D}\right)^2 \left(\frac{1}{\Delta\,\omega_C}\right)^{<1} \tag{5.21}$$

for saturated pumping. Note that PS has the same dependence on the Doppler and collisional widths, see Eq.s (4.17-4.18).

It has been suggested that the angular momentum dependence (the *J*-dependence, always appears as a geometrical factor *G(J)*) should be considered in the DFWM signal interpretation, especially in DFWM thermometry [92]. However, this conclusion is based on perturbation theory, and is, therefore, only valid within the confines of a weak field. In the condition of a strong field, the angular momentum dependence needs further investigation. The *G(J)* factor should be included in multiplex DFWM interpretation where a saturating pump is hard to achieve.

5.2 Experimental set-up

A schematic view of the mid-infrared DFWM developed in this thesis is shown in Figure 5-2. The laser source, beam optimizer and signal capturing parts are similar to those in the IRPS set-up shown in Figure 4-6, and their detailed descriptions are given in *Chapter 3*. The key part of this set-up is the novel beam splitter, BP, located in the dashed box in Figure 5-2 and described in *Chapter* 3.

Out of a single laser beam, BP produces four parallel beams, each of which is on one of the corners of a 12×12 mm^2 rectangle with almost equal intensity. Three of the four beams, working as two pump beams and a probe beam, are focused together through a CaF_2 lens (f = 500 mm) into the probe volume, automatically satisfying the phase matching in the FPG geometry as shown in Figure 5-2. After

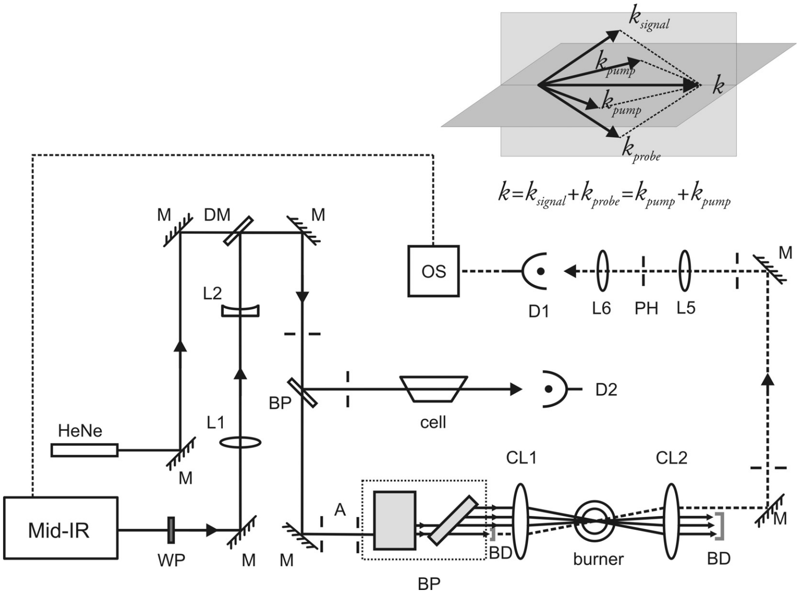

Figure 5-2 Schematic diagram of the IR-DFWM experimental arrangement. M, golden mirror; L, CaF_2 lens; DM, dichroic mirror; BP, Beam splitter (CaF_2 plate); A, aperture; BP, the beam splitter; PH, pin-hole; D, InSb detector; BD, beam dump; OS, digital oscilloscope. Signal from D2 is also input to OS that is synchronized with laser. The phase matching geometry is shown at top right.

the probe volume all the laser beams and the produced signal are collected by another CaF_2 lens (f = 500 mm), but only the signal beam is led into the InSb detector. In this set-up, the probe volume is estimated to be approximately $0.4\times0.4\times10$ mm^3.

The great advantage of this design is the much easier optical alignment. The two fixed apertures before the BP are designed to lock the direction of the incident beam. This design substantially facilitates the alignment process, especially in the mid-infrared spectral range, where visible beam indicators are lacking.

5.3 Application for thermometry

The IR-DFWM set-up was initially demonstrated for measurements of HCl and C_2H_2 in cold flows (see *Paper* III). The sensitivity of this IR-DFWM set-up was found to be roughly the same as that of the IRPS for these two cold gases, approximately 30 ppm (at 297 K and 1 bar). The recording line shapes of the C_2H_2 P(11) line at around 3255 cm^{-1} at atmospheric and low pressures using

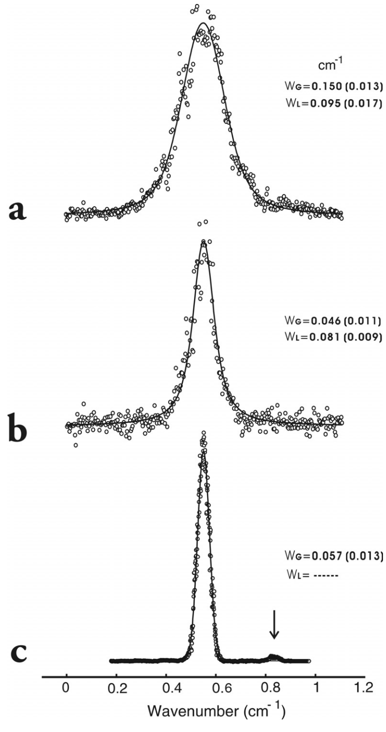

Figure 5-3 *IR-DFWM line shapes of the P(11) line at different laser energies and pressures.* ***(a)*** *I = 2.0 mJ and P = 1 bar;* ***(b)*** *I = 0.20 mJ and P = 1 bar and* ***(c)*** *I = 0.20 mJ and P = 50 mbar.* ***(a)*** *and* ***(b)*** *were obtained at a concentration of 150 ppm* C_2H_2*, whereas* ***(c)*** *was measured at a concentration of 4000 ppm* C_2H_2 *in a low pressure cell. The circles represent measured values, and the solid lines are fitted Voigt profiles. The line profile is broadened by high laser power and collision effects, and in flames due to the less collision, the line width is narrower than that at room temperature.*

saturating and nonsaturating beams are shown in Figure 5-3. The line profile was broadened with high laser power and collision effects. The same relationship of line width with pressure and laser power is found in IRPS. Note that this IR-DFWM, as well as the IRPS, is not in counter propagation geometry, meaning that it is not sub-Doppler.

The hot water lines in flames are broadly distributed and the relative line intensities vary dramatically between neighboring lines with temperature [38], following the Boltzmann distribution; see Figure 5-4. Water is generally available in combustion environments, which prompts the use of the ratios between two lines of H_2O in the IR-DFWM or IRPS spectra for temperature measurements.

The IR-DFWM spectra of H_2O were recorded in a homogenous gas flow with different temperatures; ranging from 1000 K to near to 2000 K. Three water IR-DWFM spectral bands, i.e. B1, B2 and B3, were chosen to measure the temperature dependence. The band peak intensity ratios are shown in Figure 5-5 as a function of temperature. The intensity ratio between bands, B2/B3, changes more than 200 times from 1000 K to 1900 K, which provides a very sensitive thermometer, especially in the range of 1000 – 1500 K. For the same group of spectral lines, IR-DFWM thermometry is two times more sensitive than linear optical techniques, like absorption spectroscopy [58-62].

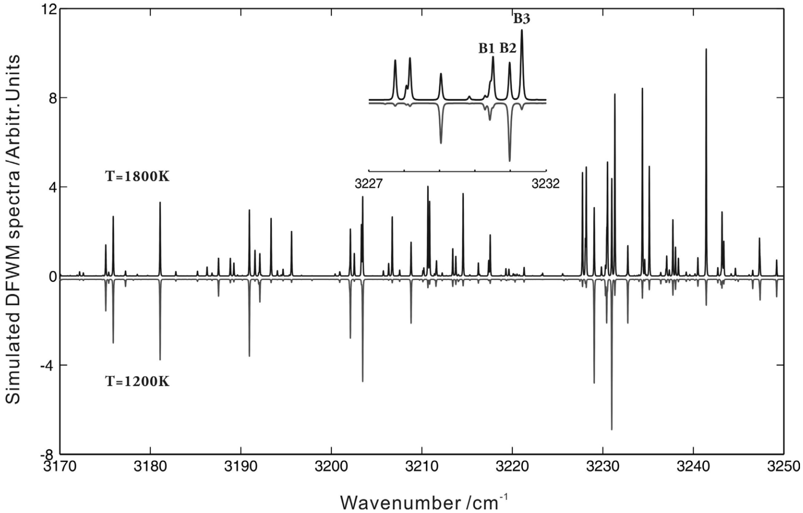

Figure 5-4 *Simulated H_2O IR-DFWM spectra at 1800 K and 1200 K based on the HITEMP 2010 database using μ^4 dependence. The insert shows the change of line intensity ratio with temperature and it is also the spectral range of performing measurements. In bands of B1 and B3 there is more than one single spectral line.*

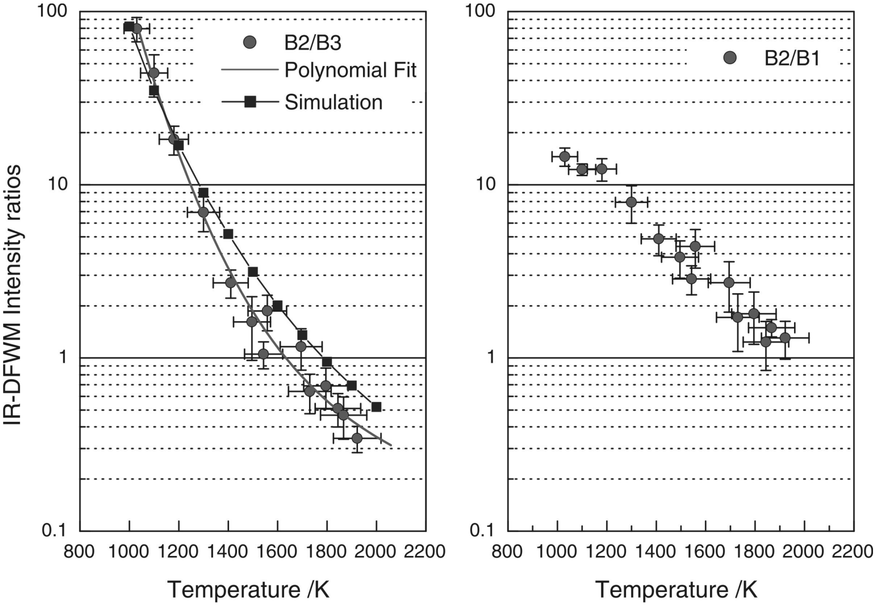

Figure 5-5 *Peak intensity ratios of B2/B3 and B2/B1; The ratio of B2/B3 was chosen as temperature sensor in this thesis, for which a 3 order polynomial fit (red line) was performed. The ratio of B2/B3 was simulated based on HITEMP2000 and is shown as well.*

Although the IR-DFWM of H_2O shows potential for use in temperature measurement, its use as an effective requires further investigation. As shown in Figure 5-5, at high temperatures the measure ratios differ from the simulated ones. It might be due to the different *J*-dependence for different lines, since the *G(J)* factor was not considered in the simulation conducted here. Moreover, it is possible that the deviation between the simulated and the measured ratios could be the result of the assumption of μ^4 dependence of the signal. Eq.s (5.13-5.14) express the dependence of the signal intensity on the transition dipole moment, but they are valid only for two extreme limits of laser power. The variation of the dependence of the DFWM signal on transition dipole moment with laser power complicates signal interpretation. Moreover, the pulsed laser is not really monochromatic, which might also be a source of the uncertainty illustrated in Figure 5-5.

This technique might also find better application in low pressure flames, for which non-intrusive thermometry continues to be challenging. The use of the IRPS of hot H_2O lines for thermometry in combustion is also promising and attractive since IRPS signal intensity maintains the $\sigma_{JJ_1}^2$ relation under different laser powers, which should greatly simplify signal interpretation.

Chapter 6

Summary and outlook

Polarization spectroscopy was successfully applied in the infrared spectral range in this thesis work and it has been developed for quantitative measurements of key hydrocarbon molecule (C_2H_2) in sooty flames and toxic species (HCl, HCN and HF) in not only particle-free flames but also particle-laden combustion environments. Single-shot imaging using IRPS has been demonstrated. In terms of infrared Degenerate Four-wave Mixing, a convenient set-up was developed and used for flame thermometry by probing line intensity ratios from the H_2O molecule.

The basic knowledge needed to understand PS and DFWM, and to complete related projects, is summarized in this thesis. Research published and achievements related to both IRPS and IR-DFWM have been briefly introduced. Both techniques are proved to be promising diagnostics for measurements of infrared-active species in combustion and other harsh environments. They can be used, for example, to study gaseous molecular spectroscopy and for measurements in plasma.

In the future, it should prove attractive to apply IRPS to low pressure (50 mbar) flames for quantitative measurements where the collision effect is less severe than in atmospheric and high pressure situations. The flame reaction zone is much thicker at low pressure than that at atmospheric pressure, which enables spatially resolved measurements across the reaction zone where rich intermediates exist. Also noteworthy, due to the relatively low molecular number density at low pressure, the beam steering and dispersion effect can be greatly reduced.

Temperature measurement in low pressure flames using optical technique remains challenging. The low molecular number density always results in a low signal-to-noise (S/N) ratio, and therefore low accuracy in terms of temperature measurements. Because it can provide high S/N H_2O spectra in low pressure flames, the development of IRPS for thermometry in these flames is a very attractive proposition. Application of IRPS in sooty flames or particle-laden combustion environments would also be a valuable development.

Compared to IRPS, IR-DFWM is more suitable for applications to environments with elevated pressures since IR-DFWM can afford the presence of optical windows. Broadband or multiplex IR-DFWM of H_2O offers the promise of single-shot temperature measurement in combustion.

Both IRPS and IR-DFWM can potentially be developed for new species detection in combustion applications with a tunable IR laser source. In addition, there exist opportunities to improve the accuracy and precision of these two techniques for quantitative measurements. The task not only requires the understanding of the dependencies of signal strength on various parameters, such as pressure and temperature, but also requires the development of more ideal infrared laser sources. A stable single-mode IR laser with high-quality beam profile would be useful.

References

[1] *Key world Energy Statistics*, IEA: International Energy Agency, 2011.

[2] P. Saxena and F.A. Williams, *Testing a small detailed chemical-kinetic mechanism for the combustion of hydrogen and carbon monoxide*, Combustion and Flame **145** (1-2) (2006) 316-323.

[3] A.H. Epstein, *Aircraft engines' needs from combustion science and engineering*, Combustion and Flame **159** (5) (2012) 1791-1792.

[4] M. Aldén, J. Bood, Z.S. Li and M. Richter, *Visualization and understanding of combustion processes using spatially and temporally resolved laser diagnostic techniques*, Proceedings of the Combustion Institute **33** (2011) 69-97.

[5] C.N. Banwell and E.M. McCash, *Foudamentals of molelecular spectroscopy*, The McGraw-Hill Publishing Company, London, 1994

[6] S. Svanberg, *Atomic and Molecular Spectroscopy*, Springer-Verlag, Berlin Heidelberg, 2004

[7] L.S. Rothman, I.E. Gordon, A. Barbe, D.C. Benner, P.E. Bernath, M. Birk, et al., *The HITRAN 2008 molecular spectroscopic database*, Journal of Quantitative Spectroscopy & Radiative Transfer **110** (9-10) (2009) 533-572.

[8] L.S. Rothman, C.P. Rinsland, A. Goldman, S.T. Massie, D.P. Edwards, J.M. Flaud, et al., *The HITRAN molecular spectroscopic database and HAWKS (HITRAN Atmospheric Workstation): 1996 edition*, Journal of Quantitative Spectroscopy & Radiative Transfer **60** (5) (1998) 665-710.

[9] L.S. Rothman, I.E. Gordon, R.J. Barber, H. Dothe, R.R. Gamache, A. Goldman, et al., *HITEMP, the high-temperature molecular spectroscopic database*, Journal of Quantitative Spectroscopy & Radiative Transfer **111** (15) (2010) 2139-2150.

[10] L.S. Rothman, R.B. Wattson and R.R. Gamache, *HITRAN HAWKS and HITEMP high-temperature molecular database*, Atmospheric Propagation and Remote Sensing Iv **2471** (1995) 105-111.

[11] M.L. Dubernet, V. Boudon, J.L. Culhane, M.S. Dimitrijevic, A.Z. Fazliev, C. Joblin, et al., *Virtual atomic and molecular data centre*, Journal of Quantitative Spectroscopy & Radiative Transfer **111** (15) (2010) 2151-2159.

[12] Z.S. Li, M. Rupinski, J. Zetterberg, Z.T. Alwahabi and M. Aldén, *Mid-infrared polarization spectroscopy of polyatomic molecules: Detection of nascent* CO_2 *and* H_2O *in atmospheric pressure flames*, Chemical Physics Letters **407** (4-6) (2005) 243-248.

[13] A.J. Grant, P. Ewart and C.R. Stone, *Detection of NO in a spark-ignition research engine using degenerate four-wave mixing*, Applied Physics B-Lasers and Optics **74** (1) (2002) 105-110.

[14] R. Stevens, P. Ewart, H. Ma and C.R. Stone, *Measurement of nitric oxide concentration in a spark-ignition engine using degenerate four-wave mixing*, Combustion and Flame **148** (4) (2007) 223-233.

[15] Holthuis & Associates. http://flatflame.com

[16] C. Wieman and T.W. Hänsch, *Doppler-free laser polarization spectroscopy*, Physical Review Letters **36** (20) (1976) 1170-1173.

[17] W.E. Ernst, *Doppler-free polarization spectroscopy of diatomic-molecules in flame reactions*, Optics Communications **44** (3) (1983) 159-164.

[18] W.G. Tong and E.S. Yeung, *Polarization spectroscopy for elemental analysis at trace concentrations*, Analytical Chemistry **57** (1) (1985) 70-73.

[19] G. Zizak, J. Lanauze and J.D. Winefordner, *Cross-beam polarization in flames with a pulsed dye laser*, Applied Optics **25** (18) (1986) 3242-3246.

[20] K. Nyholm, M. Kaivola and C.G. Aminoff, *Polarization spectroscopy applied to* C_2 *detection in a alame*, Applied Physics B-Lasers and Optics **60** (1) (1995) 5-10.

[21] K. Nyholm, R. Fritzon and M. Aldén, *2-Dimensional Imaging of OH in Flames by Use of Polarization Spectroscopy*, Optics Letters **18** (19) (1993) 1672-1674.

[22] K. Nyholm, R. Maier, C.G. Aminoff and M. Kaivola, *Detection of OH in Flames by Using Polarization Spectroscopy*, Applied Optics **32** (6) (1993) 919-924.

[23] A. Dreizler, R. Tadday, A.A. Suvernev, M. Himmelhaus, T. Dreier and P. Foggi, *Measurement of orientational relaxation-times of OH in a flame using picosecond time-resolved polarization spectroscopy*, Chemical Physics Letters **240** (4) (1995) 315-323.

[24] A.A. Suvernev, A. Dreizler, T. Dreier and J. Wolfrum, *Polarization-Spectroscopic Measurement and Spectral Simulation of OH* ($A^2\Sigma$ - $X^2\Pi$) *and NH* ($A^3\Pi$ - $X^3\Sigma$) *Transitions in Atmospheric-Pressure Flames*, Applied Physics B-Lasers and Optics **61** (5) (1995) 421-427.

[25] B. Lofstedt and M. Aldén, *Simultaneous detection of OH and NO in a flame using polarization spectroscopy*, Optics Communications **124** (3-4) (1996) 251-257.

[26] K. Nyholm, R. Fritzon, N. Georgiev and M. Aldén, *Two-photon induced polarization spectroscopy applied to the detection of* NH_3 *and CO molecules incold flows and flames*, Optics Communications **114** (1-2) (1995) 76-82.

[27] A. Dreizler, T. Dreier and J. Wolfrum, *Polarization spectroscopic measurement of the NH* ($A^3\Pi$ - $X^3\Sigma$) *transition in an ammonia-oxygen Flame*, Journal of Molecular Structure **349** (1995) 285-288.

[28] A.J. Duncan, Z.A. Sheikh, H.J. Beyer and H. Kleinpoppen, *Two-photon polarization Fourier spectroscopy of metastable atomic hydrogen*, Journal of Physics B-Atomic Molecular and Optical Physics **30** (5) (1997) 1347-1359.

[29] A.B. Gonzalo, K. Grutzmacher, M.I. de la Rosa, M. Steiger and A. Steiger, *Mapping of the atomic hydrogen density in combustion processes at atmospheric pressure by two-photon polarization spectroscopy*, Spectral Line Shapes, Vol 11 **559** (2001) 199-201.

[30] K. Grutzmacher, M.I. de la Rosa, A.B. Gonzalo, M. Steiger and A. Steiger, *Two-photon polarization spectroscopy applied for quantitative measurements of atomic hydrogen in atmospheric pressure flames*, Applied Physics B-Lasers and Optics **76** (7) (2003) 775-785.

[31] A. Steiger, M.I. de la Rosab, K. Grutzmacher, A.B. Gonzalo and M. Steiger, *Combustion diagnostic by quantitative two-photon polarization*

spectroscopy of atomic hydrogen, Optical Measurement Systems for Industrial Inspection Iii **5144** (2003) 818-822.

[32] W.D. Kulatilaka, R.P. Lucht, S.F. Hanna and V.R. Katta, *Two-color, two-photon laser-induced polarization spectroscopy (LIPS) measurements of atomic hydrogen in near-adiabatic, atmospheric pressure hydrogen/air flames*, Combustion and Flame **137** (4) (2004) 523-537.

[33] C.F. Kaminski and T. Dreier, *Investigation of two-photon-induced polarization spectroscopy of the a-X (1,0) transition in molecular nitrogen at elevated pressures*, Applied Optics **39** (6) (2000) 1042-1048.

[34] B. Lofstedt, R. Fritzon and M. Aldén, *Investigation of NO detection in flames by the use of polarization spectroscopy*, Applied Optics **35** (12) (1996) 2140-2146.

[35] Z.S. Li, M. Rupinski, J. Zetterberg, Z.T. Alwahabi and M. Aldén, *Detection of methane with mid-infrared polarization spectroscopy*, Applied Physics B-Lasers and Optics **79** (2) (2004) 135-138.

[36] Z.S. Li, M. Linvin, J. Zetterberg, J. Kiefer and M. Aldén, *Mid-infrared polarization spectroscopy of C_2H_2: Non-intrusive spatial-resolved measurements of polyatomic hydrocarbon molecules for combustion diagnostics*, Proceedings of the Combustion Institute **31** (2007) 817-824.

[37] Z.S. Li, M. Rupinski, J. Zetterberg and M. Aldén, *Mid-infrared PS and LIF detection of CH_4 and C_2H_6 in cold flows and flames at atmospheric pressure*, Proceedings of the Combustion Institute **30** (2005) 1629-1636.

[38] Z.S. Li, C.H. Hu, J. Zetterberg, M. Linvin and M. Aldén, *Midinfrared polarization spectroscopy of OH and hot water in low pressure lean premixed flames*, Journal of Chemical Physics **127** (8) (2007) 084310.

[39] A.J. Bain, P.J. Mccarthy and R.M. Hochstrasser, *Picosecond polarization spectroscopy as a probe of intramolecular dynamics - rovibronic relaxation in the S1 State of Trans-Stilbene*, Chemical Physics Letters **125** (4) (1986) 307-312.

[40] R. Tadday, A. Dreizler, A.A. Suvernev and T. Dreier, *Measurement of orientational relaxation times of OH ($A^2\Sigma$ - $X^2\Pi$) transitions in atmospheric pressure flames using picosecond time-resolved non-linear spectroscopy*, Journal of Molecular Structure **410** (1997) 85-88.

[41] R. Tadday, A.A. Suvernev, T. Dreier and J. Wolfrum, *Quantum beat spectroscopy of OH radicals in atmospheric pressure flames*, Chemical Physics Letters **268** (1-2) (1997) 117-124.

[42] J. Reppel and Z.T. Alwahabi, *Orthogonal planar laser polarization spectroscopy*, Applied Optics **41** (21) (2002) 4267-4272.

[43] M. Linvin, Z.S. Li, J. Zetterberg and M. Aldén, *Single-shot imaging of ground-state hydrogen atoms with a non-linear laser spectroscopic technique*, Optics Letters **32** (11) (2007) 1569-1571.

[44] K. Nyholm, R. Fritzon and M. Aldén, *Single-pulse two-dimensional temperature imaging in flames by degenerate four-wave mixing and polarization spectroscopy*, Applied Physics B-Lasers and Optics **59** (1) (1994) 37-43.

[45] K. Nyholm, *Measurements of OH rotational temperatures in flames by using polarization spectroscopy*, Optics Communications **111** (1-2) (1994) 66-70.

[46] R.E. Teets, F.V. Kowalski, W.T. Hill, N. Carlson and T.W. Hänsch, *Advances in Laser Spectroscopy I, SPIE Proceedings Volume 113*, Bellingham, WA: Society for Photo-Optical Instrumentation Engineers, 1977

[47] W. Demtröder, *Laser Spectroscopy Vol. 2: Experimental Techniques*, Springer-Verlag, Berlin, 2008

[48] T.B. Settersten, R.L. Farrow and J.A. Gray, *Coherent infrared-ultraviolet double-resonance spectroscopy of* CH_3, Chemical Physics Letters **370** (1-2) (2003) 204-210.

[49] T.B. Settersten, R.L. Farrow and J.A. Gray, *Infrared-ultraviolet double-resonance spectroscopy of OH in a flame*, Chemical Physics Letters **369** (5-6) (2003) 584-590.

[50] T.A. Reichardt and R.P. Lucht, *Theoretical calculation of line shapes and saturation effects in polarization spectroscopy*, Journal of Chemical Physics **109** (14) (1998) 5830-5843.

[51] W.C. Giancola, T.A. Reichardt and R.P. Lucht, *Multi-axial-mode laser effects in polarization spectroscopy*, Journal of the Optical Society of America B-Optical Physics **17** (10) (2000) 1781-1794.

[52] J. Walewski, C.F. Kaminski, S.F. Hanna and R.P. Lucht, *Dependence of partially saturated polarization spectroscopy signals on pump intensity and collision rate*, Physical Review A **64** (6) (2001).

[53] S. Roy, R.P. Lucht and J.R. Gord, *Dynamics of the moments of angular momentum distribution during generation of laser-induced polarization spectroscopy (LIPS) signal*, Journal of the Optical Society of America B-Optical Physics **28** (2) (2011) 208-219.

[54] T.A. Reichardt, F. Di Teodoro, R.L. Farrow, S. Roy and R.P. Lucht, *Collisional dependence of polarization spectroscopy with a picosecond laser*, Journal of Chemical Physics **113** (6) (2000) 2263-2269.

[55] M.L. Costen, H.J. Crichton and K.G. McKendrick, *Measurement of orientation and alignment moment relaxation by polarization spectroscopy: Theory and experiment*, Journal of Chemical Physics **120** (17) (2004) 7910-7926.

[56] S. Roy, R.P. Lucht and T.A. Reichardt, *Polarization spectroscopy using short-pulse lasers: Theoretical analysis*, Journal of Chemical Physics **116** (2) (2002) 571-580.

[57] Z.W. Sun, Z.S. Li, B. Li, Z.T. Alwahabi and M. Aldén, *Quantitative C_2H_2 measurements in sooty flames using mid-infrared polarization spectroscopy*, Applied Physics B-Lasers and Optics **101** (1-2) (2010) 423-432.

[58] W. Ren, J.B. Jeffries and R.K. Hanson, *Temperature sensing in shock-heated evaporating aerosol using wavelength-modulation absorption spectroscopy of CO_2 near 2.7 mu m*, Measurement Science & Technology **21** (10) (2010) 105603.

[59] A. Farooq, J.B. Jeffries and R.K. Hanson, *CO_2 concentration and temperature sensor for combustion gases using diode-laser absorption near 2.7 mu m*, Applied Physics B-Lasers and Optics **90** (3-4) (2008) 619-628.

[60] A. Farooq, J.B. Jeffries and R.K. Hanson, *In situ combustion measurements of H_2O and temperature near 2.5 mu m using tunable diode laser absorption*, Measurement Science & Technology **19** (7) (2008) 075604.

[61] X. Zhou, J.B. Jeffries and R.K. Hanson, *Development of a fast temperature sensor for combustion gases using a single tunable diode laser*, Applied Physics B-Lasers and Optics **81** (5) (2005) 711-722.

[62] X. Zhou, X. Liu, J.B. Jeffries and R.K. Hanson, *Development of a sensor for temperature and water concentration in combustion gases using a single tunable diode laser*, Measurement Science & Technology **14** (8) (2003) 1459-1468.

[63] P. Ewart and S.V. Oleary, *Comparisons of sodium: rare-gas potentials by measurements of excited-state degenerate fuor-wave mixing*, Journal of Physics B-Atomic Molecular and Optical Physics **15** (20) (1982) 3669-3677.

[64] J. Pender and L. Hesselink, *Phase conjugation in a flame*, Optics Letters **10** (6) (1985) 264-266.

[65] P. Ewart and S.V. Oleary, *Detection of OH in a flame by degenerate four-wave mixing*, Optics Letters **11** (5) (1986) 279-281.

[66] T. Dreier and D.J. Rakestraw, *Degenerate four-wave mixing diagnostics on OH and NH radicals in flames*, Applied Physics B-Photophysics and Laser Chemistry **50** (6) (1990) 479-485.

[67] S. Williams, D.S. Green, S. Sethuraman and R.N. Zare, *Detection of trace species in hostile environments using degenerate four-wave mixing: CH in an atmospheric-pressure flame*, Journal of the American Chemical Society **114** (23) (1992) 9122-9130.

[68] D.J. Rakestraw, L.R. Thorne and T. Dreier, *Detection of NH radicals in flames using degenerate four-wave mixing*, Proceedings of the Combustion Institute **23** (1991) 1901-1907.

[69] S.J. Tsay, K.G. Owens, K.W. Aniolek, D.L. Miller and N.P. Cernansky, *Detection of CN by degenerate four-wave mixing*, Optics Letters **20** (16) (1995) 1725-1727.

[70] K. Nyholm, M. Kaivola and C.G. Aminoff, *Detection of C_2 and temperature measurement in a flame by using degenerate four-wave mixing in a forward geometry*, Optics Communications **107** (5-6) (1994) 406-410.

[71] C.F. Kaminski, I.G. Hughes and P. Ewart, *Degenerate four-wave mixing spectroscopy and spectral simulation of C_2 in an atmospheric pressure oxy-acetylene flame*, Journal of Chemical Physics **106** (13) (1997) 5324-5332.

[72] B.A. Mann, S.V. Oleary, A.G. Astill and D.A. Greenhalgh, *Degenerate four-wave mixing in nitrogen dioxide: application to combustion diagnostics*, Applied Physics B-Photophysics and Laser Chemistry **54** (4) (1992) 271-277.

[73] V. Kruger, S. Le Boiteux, Y.J. Picard and B. Attal-Tretout, *Atomic oxygen detection in flames using two-photon degenerate four-wave mixing*, Journal of Physics B-Atomic Molecular and Optical Physics **33** (15) (2000) 2887-2905.

[74] G.M. Lloyd, I.G. Hughes, R. Bratfalean and P. Ewart, *Broadband degenerate four-wave mixing of OH for flame thermometry*, Applied Physics B-Lasers and Optics **67** (1) (1998) 107-113.

[75] P. Ewart and P. Snowdon, *Multiplex degenerate four-wave mixing in a flame*, Optics Letters **15** (1990) 1403-1405.

[76] C.F. Kaminski, I.G. Hughes, G.M. Lloyd and P. Ewart, *Thermometry of an oxy-acetylene flame using multiplex degenerate four-wave mixing of C_2*, Applied Physics B-Lasers and Optics **62** (1) (1996) 39-44.

[77] H. Latzel, A. Dreizler, T. Dreier, J. Heinze, M. Dillmann, W. Stricker, et al., *Thermal grating and broadband degenerate four-wave mixing spectroscopy of OH in high-pressure flames*, Applied Physics B-Lasers and Optics **67** (5) (1998) 667-673.

[78] G.M. Lloyd and P. Ewart, *Optical dephasing effects in broadband four-wave mixing in C_2: Implications for broadband FWM thermometry*, Journal of Chemical Physics **116** (4) (2002) 1370-1379.

[79] P. Ewart, P. Snowdon and I. Magnusson, *Two-Dimensional phase-conjugate imaging of atomic distributions in flames by degenerate four-wave mixing*, Optics Letters **14** (11) (1989) 563-565.

[80] D.J. Rakestraw, R.L. Farrow and T. Dreier, *Two-dimensional imaging of OH in flames by degenerate four-wave mixing*, Optics Letters **15** (12) (1990) 709-711.

[81] P. Ewart, P.G.R. Smith and R.B. Williams, *Imaging of trace species distributions by degenerate four-wave mixing: diffraction effects, spatial resolution, and image referencing*, Applied Optics **36** (24) (1997) 5959-5968.

[82] K. Richard and P. Ewart, *High-resolution infrared polarization spectroscopy and degenerate four wave mixing spectroscopy of methane*, Applied Physics B-Lasers and Optics **94** (4) (2009) 715-723.

[83] G.J. Germann, R.L. Farrow and D.J. Rakestraw, *Infrared degenerate four-wave mixing spectroscopy of polyatomic molecules: CH_4 and C_2H_2*, Journal of the Optical Society of America B-Optical Physics **12** (1) (1995) 25-32.

[84] G.J. Germann, A. Mcilroy, T. Dreier, R.L. Farrow and D.J. Rakestraw, *Detection of polyatomic-molecules using infrared degenerate four-wave mixing*,

Berichte Der Bunsen-Gesellschaft-Physical Chemistry Chemical Physics **97** (12) (1993) 1630-1634.

[85] R.L. Farrow, D.J. Rakestraw and T. Dreier, *Investigation of the dependence of degenerate four-wave mixing line intensities on transition dipole moment*, Journal of the Optical Society of America B-Optical Physics **9** (10) (1992) 1770-1777.

[86] P.M. Danehy, E.J. Friedmanhill, R.P. Lucht and R.L. Farrow, *The effects of collisional quenching on degenerate four-wave mixing*, Applied Physics B-Photophysics and Laser Chemistry **57** (4) (1993) 243-248.

[87] R.P. Lucht, R.L. Farrow and D.J. Rakestraw, *Saturation effects in gas-phase degenerate four-wave mixing spectroscopy: nonperturbative calculations*, Journal of the Optical Society of America B-Optical Physics **10** (9) (1993) 1508-1520.

[88] R.T. Bratfalean, G.M. Lloyd and P. Ewart, *Degenerate four-wave mixing for arbitrary pump and probe intensities*, Journal of the Optical Society of America B-Optical Physics **16** (6) (1999) 952-960.

[89] T.A. Reichardt, W.C. Giancola, C.M. Shappert and R.P. Lucht, *Experimental investigation of saturated degenerate four-wave mixing for quantitative concentration measurements*, Applied Optics **38** (33) (1999) 6951-6961.

[90] T.A. Reichardt and R.P. Lucht, *Resonant degenerate four-wave mixing spectroscopy of transitions with degenerate energy levels: Saturation and polarization effects*, Journal of Chemical Physics **111** (22) (1999) 10008-10020.

[91] S. Williams, R.N. Zare and L.A. Rahn, *Reduction of degenerate four-wave mixing spectra to relative populations. 2. Strong-field limit*, Journal of Chemical Physics **101** (2) (1994) 1093-1107.

[92] D. Kupiszewska and B.J. Whitaker, *Thermometry by degenerate four-wave mixing: J dependence of laser-induced grating reflectivity*, Journal of the Chemical Society-Faraday Transactions **89** (16) (1993) 2951-2956.

[93] T.A. Reichardt and R.P. Lucht, *Effect of Doppler broadening on quantitative concentration measurements with degenerate four-wave mixing spectroscopy*, Journal of the Optical Society of America B-Optical Physics **13** (6) (1996) 1107-1119.

[94] T.A. Reichardt and R.P. Lucht, *Degenerate four-wave mixing spectroscopy with short-pulse lasers: Theoretical analysis*, Journal of the Optical Society of America B-Optical Physics **13** (12) (1996) 2807-2816.

[95] T.A. Reichardt, R.P. Lucht, P.M. Danehy and R.L. Farrow, *Theoretical investigation of the forward phase-matched geometry for degenerate four-wave mixing spectroscopy*, Journal of the Optical Society of America B-Optical Physics **15** (10) (1998) 2566-2572.

[96] S. Williams, R.N. Zare and L.A. Rahn, *Reduction of degenerate four-wave mixing spectra to relative populations. 1. Weak-field limit*, Journal of Chemical Physics **101** (2) (1994) 1072-1092.

[97] R.L. Farrow and D.J. Rakestraw, *Detection of trace molecular-species using degenerate four-wave mixing*, Science **257** (5078) (1992) 1894-1900.

[98] A.C. Eckbreth, *Laser Diagnostics for Combustion Temperature and Species*, Gordon and Breach, New York, 1996

[99] K. Kohse-Höinghaus and J.B. Jeffries, *Applied Combustion Diagnostics*, Taylor & Francis, New York, 2002

[100] J. Kiefer and P. Ewart, *Laser diagnostics and minor species detection in combustion using resonant four-wave mixing*, Progress in Energy and Combustion Science **37** (5) (2011) 525-564.

[101] R.W. Boyd, *Non-linear Optics*, Academic Press, Inc., San Diego, 1992

[102] A. Dreizler, T. Dreier and J. Wolfrum, *Thermal grating effects in Infrared degenerate four-wave mixing for trace gas detection*, Chemical Physics Letters **233** (5-6) (1995) 525-532.

[103] P.M. Danehy, P.H. Paul and R.L. Farrow, *Thermal grating contributions to degenerate four-wave mixing in NO*, Journal of the Optical Society of America B-Optical Physics **12** (9) (1995) 1564-1576.

[104] P.H. Paul, R.L. Farrow and P.M. Danehy, *Gas-phase thermal-grating contributions to four-wave mixing*, Journal of the Optical Society of America B-Optical Physics **12** (3) (1995) 384-392.

[105] P.M. Danehy and R.L. Farrow, *Comparison of degenerate four-wave mixing line shapes from population- and thermal-grating scattering*, Journal of the Optical Society of America B-Optical Physics **13** (7) (1996) 1412-1418.

[106] P.A. Delve and B.J. Whitaker, *A simple model to describe thermal grating effects in degenerate four wave mixing spectroscopy*, Physical Chemistry Chemical Physics **2** (24) (2000) 5594-5601.

[107] R.L. Abrams and R.C. Lind, *Degenerate four-wave mixing in absorbing media*, Optics Letters **2** (4) (1978) 94-96.

Acknowledgements

All work described in this thesis was carried out at Lund University in the Division of Combustion Physics. It has been a great pleasure and honour to achieve my doctoral degree in Sweden, such a friendly and beautiful country. In the past five years in Lund I got kind help in life and in study from many people, and to each of them I am sincerely grateful.

I would like to express my particular appreciation to My supervisor, Professor *Marcus Aldén*, for providing me the opportunity to work and study here, and for so much I have benefited from his deep knowledge and his long and broad experience in combustion/laser filed, and from his never-ending enthusiasm and inspiration. *Marcus* provided the frame work for my research, and he also deleted or added so many *the* in my manuscript.

Specifically, I would like to my co-supervisor, associate Professor *Zhongshan Li,* for all your support. *Li* has done most of the day-to–day supervising to me. He helps me not only in study but also in life. *Li* always introduces different interesting topics, not limited to combustion science, to us, which definitely widens my scientific knowledge. I have got scientific training from *Li* in the lab and from our *hot* discussions. I can only say is *Thank You*.

I would like to thank *Bo Li* for our close collaboration in work, for your considerable help in the past five years and for our friendship. Thanks to Dr. *Johan Zetterberg* and *Anna-Lena Sahlberg* for working together and solving many problems so effectively in the infrared laboratory. *Good luck*! even I don't think good luck can bring you anything in laboratories. Thanks to Dr. *Zayad Alwahabi* from Adelaide, Dr. *Johannes Kiefer* from Erlangen, Dr. *Nico J. Dam* from Eindhoven and Dr. *Michael Försth* from SP for our happy and fruitful collaborations. Thanks to *Ronald Whiddon*, my four years roommate, for his patience on listening my Chinese-English and his help.

I would like to thank Professor *Per-Erik Bengstsson*, Professor *Alexander Konnov*, Dr. *Mattias Richter,* Dr. *Joakim Bood,* Dr. *Frederik Ossler* for their courses on combustion/chemistry, laser-diagnostics and spectroscopy. These courses gave me background knowledge from which I benefited a lot during my work, and gave me credits I need to graduate. I am also indebted to the current and former staff at the Division of Combustion Physics, *Cecilia Bille*, *Minna Ramkull*, *Eva Persson*, *Sven-Inge Möller*, *Robert Collin*, *Anneli Nilsson Ahlm*, *Rutger Lorensson, Susanne Dunér, Nina Mårtensson,* and *Sara Holmgren* have helped me with all kinds of different matters throughout my work here.

I would also like to thank my current and former colleagues at Division of Combustion Physics, *Andreas Lantz*, *Alexis Bohlin*, *Edouard Berrocal*, *Andreas Ehn*, *Henrik Bladh*, *Olof Johansson*, *Johannes Lindén*, *Elias Kristensson, Bo Zhou*, *Jiajian Zhu*, *Zheming Li, Gustaf Särner, Christoph Knappe*, *Jonathan Johnssson*, *Billy Kaldvee*, *Malin Jonsson*, *Rikard Wellander*, *Jesper Borggren*, *Christian Brackmann*, *Linda Vallenhag*, *Nils-Erik Olofsson* and *Joakim Rosell*. They make the division a pleasant place to work at. Special thanks to*, Edouard Berrocal*, *Andreas Lantz, Vladimir Alekseev*, and *Eric Baudoin* for our happiness in football sports.

I would thank my Chinese friends, working in combustion or not, Professor *Zhihua Wang*, Professor *Xue-song Bai*, Dr. *Rixin Yu*, *Yong He*, *Fan Zhang*, *Jiangfei Yu*, *Chaoqi Xu*, *Yajing Wu*, Dr. *Mingbo Sun*, Dr. *Beibei Yan*, *Haichun Liu*, Dr. *Jian Zuo*, *Dan Xu*, Dr. *Yu Li*, Dr. *Li Yang*, *Ying Yan* and Dr. *Eric Hsu* for their help and for spending happy time with them.

I can never thank enough my mother Mrs. *Wang*, my parents-in-law Mrs. *Gong* and Mr. *Xu*, and my sisters *Lijun* and *Lihui*. They gave me so much unreserved support and understanding during these years. All words fail to express my appreciation to my beloved wife *Ya Xu*. Your love supports me every day, everywhere. My little boy, *Tiaotiao*, you are the greatest joy of Mama and Papa.

This dissertation is dedicated to my father, who guided me through drawing a house …

Summary of papers

Paper I

In this letter we reported on the measurement of HCl using IRPS. This is our first work on toxic species measurements using IRPS. A detection limit of less than 50 ppm in flames was estimated.

I did all measurements and evaluated the data. Zhongshan Li and Marcus Aldén prepared the manuscript.

Paper II

This paper is not about measurements in the infrared. A new type of two-color four-wave mixing spectroscopy of OH in the UV was demonstrated by employing a non-resonant pumping and resonant probing.

I and Bo Li did all measurements. I performed data evaluations. Johannese Kiefer and Zhongshan Li prepared the manuscript.

Paper III

A stable and convenient optical system to realize infrared DFWM was demonstrated in this paper. The key part of this work is the novel beam splitter, and the set-up was demonstrated by detection C_2H_2 and HCl in cold flow gas. A detection limit of approximately 30 ppm for C_2H_2 at 296 K and atmospheric pressure was achieved that is comparable to that of IRPS.

Zhongshan Li prepared the beam splitter and planed the experiments. Bo Li set up the beam splitter. I performed all measurements and data evaluations. I prepare the manuscript, and Zhongshan Li, Paul Ewart and Marcus Aldén improved the manuscript.

Paper IV

IRPS was applied for C_2H_2 quantitative diagnostics in sooty flames. This paper, for the first time, introduced the signal quantification in IRPS showing its capability of quantitative measurements. Meanwhile, this paper demonstrated the application of IRPS in sooty flames.

I did all measurements and Zeyad Alwahabi joined part of measurements in flames. I performed data evaluations and prepare the manuscript. Zhongshan Li and Marcus Aldén improved the manuscript.

Paper V

Quantitative measurements of HCN were performed using IRPS in atmospheric N_2O flames. The experimental results were compared with calculations performed using detailed chemistry mechanisms, which implements NCN prompt-NO reactions.

I did all measurements and evaluated the data. Alexander Konnov did chemistry numerical simulations. I, Zhongshan Li and Alexander Konnov prepared the manuscript, together.

Paper VI

The potential of infrared DFWM for temperature measurements was demonstrated in environments produced by a temperature-calibrated burner. By detecting three groups of spectral lines of H_2O, the environmental temperature can be derived from the intensity ratio of spectral lines. The experimental results had been compared with that modeled based on HITRAN database.

I did all measurements and evaluated the data. I prepared the manuscript. Zhongshan Li and Marcus Aldén improved the manuscript. Bo Li prepared the burner and measured the temperature.

Paper VII

Using IRPS, we, in-situ, measured HCl emitted from PVC carpet burning in a furnace tube. In this paper HCl was measured in a smoke environment, and the signal attenuation was measured simultaneously to compensate the signal loss.

I and Michael Försth did all measurements. I evaluated the data. I and Michael Försth prepared the manuscript but Michael did the major writing work.

Paper VIII

In this letter, two-dimensional imaging using IRPS of HF molecules was demonstrated in flames. High spatial resolution was achieved by adopting an orthogonal pump-probe geometry and as a coherent technique the strong thermal background radiation was suppressed.

I did spectral measurements by myself, and did imaging working together with Johan Zetterberg. I did all data evaluations. I prepared the original manuscript, and Zhongshan Li and Marcus Aldén improved it.

Paper IX

In this work, we demonstrated the ability of IRPS for minor species detection in hostile combustion systems where aerosol or coal/biomass particles are present. The results showed that IRPS can tolerate heavy particle in combustion. The background physics of IRPS suppressing particle scattering are discussed, as well as the possibility of quantitative measurement using IRPS.

The experimental results in this paper were from other projects I joined. Yong He and Bo Li are responsible for the projects. I did all experimental work of this paper. Anna-lena Sahlberg, Zhongshan Li and Marcus Aldén improved the writing.